



Environmental Physics Laboratory

- Research Report -

EPL-RR-1-2012

Prospects for Flash Flood Forecasting in Mountainous Regions

– An Investigation of Tropical Storm Fay in the Southern Appalachians

Jing Tao and Ana P. Barros

Citation: Tao, J., and Barros, A. P., 2012: Prospects for Flash Flood Forecasting In Mountainous Regions - An Investigation of Tropical Storm Fay in the Southern Appalachians. Duke University, Pratt School of Engineering, Hydrology and Fluid Dynamics Program, Environmental Physics Laboratory Research Report No. EPL-RR-1-2012, 80pp.

Hydrology and Fluid Mechanics Program
Civil and Environmental Engineering Department
Pratt School of Engineering – Duke University
Box 90287 – Durham, NC 27708

Publication Date History

First published on April 29, 2012

Disclaimer – EPL Research Reports are published upon submission for publication in the peer-reviewed literature and are subject to updates as reflected by the publication dates. This report was submitted to internal review, and is currently under external review in the *Journal of Hydrology*.

Abstract

The sensitivity of Quantitative flash-Flood Estimates (QFEs) and Quantitative flash-Flood Forecasts (QFFs) to Quantitative Precipitation Estimates (QPEs) and Quantitative Precipitation Forecasts (QPFs) in mountainous regions was investigated for the passage of Tropical Storm Fay, 2008 over the Southern Appalachian Mountains in North Carolina, USA. QFEs and QFFs were generated by an uncalibrated high-resolution hydrologic model ($250 \times 250 \text{ m}^2$) with coupled surface-subsurface physics and rainfall forcing from the National Severe Storms Laboratory Next Generation Multi-sensor QPE (Q2) spatial rainfall ($1 \times 1 \text{ km}^2$) product, and from the operational QPF product from the National Weather Service National Digital Forecast Database (NDFD, $5 \times 5 \text{ km}^2$). Optimal QPE products (Q2+) were derived by merging Q2 with rainfall observations from a high density raingauge network in the Great Smoky Mountains (GSMRGN) and subsequently used as “rainfall truth” to characterize operational QPF and QFE errors in three headwater catchments with different topographic and hydro-geomorphic characteristics. Deterministic QFE results agree well with observations regarding total water volume and peak flow, and with Nash-Sutcliffe coefficients 0.8-0.9 indicating that the distributed model without calibration captures well the dominant physical processes. The impact of Q2+ uncertainty with regard to the space-time structure of storm rainfall was subsequently evaluated through Monte Carlo replicates of the QPEs to generate QFE distributions. For long lasting events with several cells of heavy rainfall embedded in otherwise light to moderate rainfall such as Tropical Storms, the propagation of uncertainty from rainfall to flood response is highly non-linear, and exhibits strong dependence on basin physiography, soil moisture conditions (transient basin storage capacity), and runoff generation and conveyance mechanisms (overland flow, interflow and baseflow). The use of distributed physically-based models which can predict not only stream

discharge but also the space-time distribution of runoff components should be therefore advantageous over threshold approaches in operational quantitative flash flood forecasting and associated hazards (landslides and debris flows). The ultimate objective of this work however is to assess QFF projects in ungauged basins, and the utility of satellite data to improve short lead-time forecasts and nowcasts. To this end, operational QFF at 6-1 hour lead times during Fay was simulated using the 3D-LSHM driven by precipitation composites consisting of Q2 QPE and NDFD QPF after which showed ubiquitous lack of useful skill. Potential gains in QFF performance by merging satellite overpass observations to operational QPF were examined next for two adjacent catchments. The results show that merging of satellite observations into operational QPE/QPF could significantly improve the utility and precision of current operational QFF guidance, where the timing of heavy rainfall and satellite overpass are very close, but that the improvement depends strongly on storm-dependent and basin-specific rainfall-runoff dynamics.

Keywords:

Quantitative flash-Flood Estimate (QFE); Quantitative flash-Flood Forecast (QFF); Distributed hydrological modeling; Radar-based Quantitative Precipitation Estimate (QPE); Quantitative Precipitation Forecast(QPF); Global Precipitation Measurement (GPM) Mission.

1. Introduction

Floods are one of the major reasons for death caused by weather-related hazards in the USA, and most flood-related deaths are attributed to flash floods (Ashley and Ashley, 2008; French et al., 1983). For operational purposes, flash floods are rapid fluvial flooding events that are characterized by the time to peak of the hydrograph being less than or equal to six hours (Georgakakos and Hudlow, 1984; NWS, 2010). Flash floods are usually generated by intense and persistent rainfall and typically occur in mountainous regions, where steep slopes and small catchment areas lead to short rainfall-runoff response times. Flash floods can trigger debris flows and landslides, especially in unstable mountain slopes causing severe damage to people, infrastructure and property. There is large variability of precipitation both in space and time over complex topography, which in turn is poorly monitored by operational networks due to remoteness and difficult access (Barros, 2012; Barros and Lettenmaier, 1993; Viviroli et al., 2011). Short time-scales and space-time heterogeneity conspire to make Quantitative flash-Flood Forecasting (QFF) in mountainous regions especially challenging. The objective of this study is to investigate QFF utility over topographically complex regions using an uncalibrated physically-based fully-distributed hydrological model (3D-LSHM) forced by rainfall fields derived from Quantitative Precipitation Estimate (QPE) (Q2) and operational Quantitative Precipitation Forecast (QPF) products, and to characterize the potential benefits that timely satellite observations can provide to flash flood forecasting. In particular, the focus is on long duration events such as tropical storms characterized by transient cells of high intensity rainfall embedded within persistent light and moderate rainfall that can produce multiple flash floods and associated hazards at the regional scale.

In the United States, the accuracy of QPE has shown pronounced progress over the past decade thanks to the improvement in radar real-time precipitation retrieval techniques and the development of the ground-based Next Generation Weather Radar (NEXRAD) system, consisting of 159 Weather Surveillance Radar-1988 Doppler (WSR-88D) across the USA, and currently in the process of being upgraded to dual-polarization (<http://www.roc.noaa.gov/WSR88D/dualpol>). However, radar-based QPE is strongly affected by systematic radar noise, the quality of retrieval algorithms (e.g. the Z-R (reflectivity-rainfall) relationships), and terrain complexity (e.g. over-shooting effects when radars scan well above the terrain and the radar beams miss low-level rainfall, and ground clutter effects otherwise), resulting in significant overestimation or underestimation of precipitation (Prat and Barros, 2010a; Borga and Tonelli, 2000; Smith and Krajewski, 1991; Smith et al., 1996; Steiner et al., 1999; Young et al., 1999). Although many adjustment methods have been developed and applied to improve radar-based QPE, such as the probability matching method (Rosenfeld et al., 1994; Rosenfeld et al., 1993), mean field bias correction (Seo et al., 1999; Seo and Smith, 1992; Smith and Krajewski, 1991; Steiner et al., 1999), radar-gauge merging methods (Seo, 1998a; Seo, 1998b), and local gauge bias correction (Seo et al., 2000; Seo and Breidenbach, 2002), the question of space-time non-stationary of precipitation over topographically complex terrain remains largely to unresolved. Furthermore, despite recent NWP (Numerical Weather Prediction) improvements, including data assimilation and higher spatial resolution, QPF skill at the time (< 6 hours) and spatial scales that matter in mountainous regions remain largely inadequate (Ebert and McBride, 2000; Gourley et al., 2012; Olson et al., 1995). Additionally, fast evolution of convective systems (such as tropical storms and mesoscale convective systems) coupled with orographic effects that enhance the spatial variability of precipitation significantly further

compounds the challenge (Sun and Barros, 2012). Indeed, the NWP-based forecast skill of convective rainfall at the sub-daily (storm time-scale) even in relatively flat areas is very low (e.g. Tao and Barros, 2010). Automated Flood Warning Systems (<http://afws.erh.noaa.gov/afws/>) consisting of raingauges that detect high intensity rainfall near the ground surface remain the most effective approach to guide flash-flood warnings in remote mountainous regions (for example, there are only 53 such gauges at elevations above 1,000 m in the Appalachian Mountains in North Carolina). AFWS gauge networks tend to be placed upstream of highly populated areas where flash-floods are expected based on climatology, however because the data are used for issuing (mainly qualitative) public safety warnings, the low accuracy and sparseness of such networks limits their applicability for QPE purposes. Reed et al. (2007) provide a review of various approaches to flash flood forecasting and operational Flash Flood Guidance used to issue public warnings, and proposed the use of a distributed model and an improved threshold frequency based approach to improve operational QFF skill at ungauged locations. They also addressed the question of flood forecasting skill using calibrated versus uncalibrated hydrologic models. Because model calibration is highly sensitive to the space-time accuracy of the precipitation forcing (e.g. Bindlish and Barros, 2002), which is highly nonstationary at the spatial scales of flash-floods, and more so in complex terrain (e.g. Zocatelli et al. 2010), understanding the actual skill of QFF and QFE operations independent of the rainfall used for model calibration remains a daunting challenge (Looper et al., 2012; Gourley et al. 2011). Generally, there is broad agreement that rainfall and its organization in space and time is the necessary, though not sufficient, condition to robust flood forecasting skill. It is further necessary, however, to transfer rainfall to runoff response. In ungauged basins, only physically-based models unencumbered by calibration offer the prospect of useful predictability.

High-density, high-accuracy rainfall monitoring networks such as the Precipitation Measurement Mission (PMM) gauge network in the Great Smoky Mountains (Prat and Barros, 2010a) offer an optimal path to QPE that can be evaluated through water balance accounting at different temporal and spatial scales using river discharge observations, as well as soil moisture data, surface flux estimates from hydrometeorological towers and soil moisture observations when available. However, installation and maintenance costs of high density science grade rain gauge networks or small radars in the inner regions of complex topography are prohibitive, and in some cases not realistically possible to maintain or access. Satellite based observations of precipitation (e.g. TRMM –Tropical Rainfall Measurement Mission and the upcoming GPM-Global Precipitation Measurement Mission) are the alternative path for rainfall monitoring. Limitations of satellite-based observations include satellite revisit time (temporal sampling), spatial resolution (at best on the order of 2-4 km or larger), and, not unlike any other sensor, measurement error and retrieval error (Ebert et al., 2007; Huffman et al., 2007; Tao and Barros, 2010). On the other hand, satellite-based observations are available globally including the vast array of ungauged basins around the world. There is great optimism in operational hydrology with regard to the potential of frequent satellite-based precipitation observations to improve flood forecasting performance that is critical to address flood warning and emergency management challenges due to the small time-scales associated with floods (e.g., Collier, 2007; Wardah et al., 2008).

In this study, we conduct an assessment of current operational QFF skill in mountainous regions, and investigate the potential benefits of the upcoming GPM mission. A note of caution is warranted to explain that the research presented here was not conducted in the precise context under which actual operational forecasts are made in the United States or elsewhere, which

typically relies on regionally customized forecasting tools as well as expert forecasters. Rather, the research presented here is representative of the state-of-the-science from data and modeling points of view. First, we improve on an existing high-resolution (1km²) QPE product, Q2 (Next generation QPE, reference (Vasiloff et al., 2007), using information from its space-time error structure estimated from raingauge data in the Great Smoky Mountains. This enables documenting the sensitivity of flood response in catchments with different geomorphic and hydrogeological properties to the space-time variability of rainfall. QFE and QFF skill are evaluated by comparing hydrologic simulations using existing QPE and QPF against those obtained using the improved QPE. Furthermore, we investigate the utilization of satellite information for improving flash flood forecasts. We will examine the value of merging satellite rainfall products, specifically simulated GPM-like (Global Precipitation Measurement mission) products, and operational QPE to improve the utility of flash flood forecasting.

In the United States, River Forecast Centers (RFCs) rely on deterministic hydrologic models for both estimating and predicting flash floods. In very small basins, warnings are made based on whether event cumulative rainfall has reached a certain threshold. Hydrological models used for flood modeling encompass the so-called “black-box” data-driven models, lumped-conceptual models, and physically-based distributed hydrological models. Lumped-conceptual models currently are the most commonly used for operational flood modeling and forecasting due to their simplicity. Physically-based and fully-distributed hydrological models in principle do not require calibration because physical parameters can be explicitly derived from ancillary data (if available), thus lowering the danger of over-parameterization that is inescapable for both lumped-conceptual models and semi-distributed hydrologic models. Carpenter and Georgakakos (2006) and Moore et al. (2006) have demonstrated that physically-based distributed hydrological

models show superior performance in the case of extreme flood events than lumped rainfall-runoff models. Smith et al. (2012) conducted an extensive multi-model intercomparison and concluded that 1) calibrated distributed models provided improved hydrograph simulations compared to calibrated lumped models especially in interior basins with the added value of simulating spatially distributed soil moisture fields and observing the water balance; and 2) some uncalibrated distributed models perform better than calibrated distributed models. Here, we rely on a high-resolution distributed Land-Surface Hydrological Model (3D-LSHM) with coupled surface-subsurface physics that was used previously in the Appalachians with success (Yildiz and Barros, 2005, 2007 and 2009) to elucidate the predictability of flash floods in the Great Smoky Mountains as described above. In particular, we focus on the case of Tropical Storm Fay in August 2008 which caused extensive flooding, deaths and much damage in the South East and Mid-Atlantic states (Verdi and Holt, 2010).

The organization of the manuscript is as follows. Section 2 describes the study area and the storm event of interest. Section 3 describes the hydrologic model and essential forcing data. Section 4 describes the rainfall datasets used in this study, including raingauge observations, and Q2 and the National Digital Forecast Database (NDFD) QPF products, as well as error analysis. Two adjustment techniques aimed at improving accuracy of Q2 are proposed based on the error analysis. The spatial-temporal downscaling method applied to Q2 and QPF products to the spatial and temporal resolution required for the flood simulation is also described in Section 4. Section 5 presents the QFE experiments over three headwater catchments driven by Q2 and adjusted Q2 rainfall fields, including uncertainty analyses through Monte Carlo simulations. Section 6 discusses the QFF simulations produced by the 3D-LSHM driven by the combination of QPE and QPF, with emphasis on discussing the possibility of predicting flash flood accurately

and improving QFF by incorporating satellite information into QPE in near real-time. The quantitative evaluation of QFE and QFF are given in Section 7. Section 8 consists of Summary and Discussion.

2. Case Study

2.1 Study area

Flash-flood events are frequent in areas of steep terrain in the western U.S. and the Appalachians, with basin size ranging from 10 to 125km² (Kelsch, 2002) and larger headwater catchments (< 300 km²) depending on basin hydro-geomorphic characteristics which can strongly affect rainfall-runoff response times (e.g. Reed et al. 2007, Zoccatelli et al. 2010). In this study, we focus on three headwater catchments of the Pigeon River over Haywood County located in the Southern Appalachians in North Carolina, USA. The Pigeon River flows northwest through the county and into Tennessee, where it becomes a tributary of the French Broad River and the Little Tennessee. Considering flood records, catchment size and the existence of various dams in Haywood County, three small headwater basins were selected for this study: the Cataloochee Creek Basin (CCB) in the Great Smoky Mountains National Park, the West Fork Pigeon River Basin (WFPRB) and the East Fork Pigeon River Basin (EFPRB), delineated in black polygons in Figure 1. The WFPRB and EFPRB have drainage areas of 71km² and 131km², respectively. The Cataloochee Creek is a small tributary to the Pigeon River with a drainage area of 128km². Stream gauges at the outlet of each of the three basins are regularly maintained by the USGS (United States Geological Survey). The Pigeon River basin landscape is characterized by intermediate and high mountains covered by very dense forest, with gentle to very steep slopes, with elevations ranging between 400m and 2,000m (Figure 1). Terraces and flood plains have

slopes ranging from nearly level to moderately steep. Compared to the WFPRB and EFPRB, the CCB features relatively flat slopes and deep soils, including substantial alluvial deposits built over time due to intense landslide activity. The major soil types are Edneyville-Chestnut complex soil, Plott fine sandy loam, Wayah sandy loam and eroded Wayah loam soil (Allison et al., 1997). The spatial distribution of dominant soil texture extracted from the State Soil Geographic (STATSGO) database over Haywood County is shown Figure 2 (left), and the dominant vegetation is deciduous and mixed forest as shown by the land cover map in Figure 2 (right). The climate over the study area is subject to moisture-rich winds from the Gulf of Mexico and varies greatly from the high mountains to the flood plains along rivers. Antecedent research has demonstrated that the orographic rainfall enhancement is on the order of 60% at ridge locations compared with valley locations for concurrent rain events (Prat and Barros, 2010a). The historical average annual precipitation is ranges between 1060 mm and 2000 mm, evenly distributed throughout the year (Allison et al., 1997). Landslide hazard risk assessments indicate that up to 50% of the area of the Pigeon River is highly unstable, and that value increases up to 80-90% for the three headwater catchments examined here (Witt, 2005).

2.2 Tropical Storm Fay

Tropical Storm Fay originated from a tropical wave off the coast of Africa on August 7th, 2008, and it developed into a very strong as it moved westward across the Atlantic causing heavy rainfall in Florida and in the Southeast US generally (Verdi and Holt, 2010). Although the storm already had weakened before reaching North Carolina, its remnants produced widespread flooding in the Piedmont and in the Appalachians due to prolonged and heavy rainfall over a four-day period on August 25th -28th, 2008. The total storm rainfall amounts were close to 100mm (~ 4 in) over the northern ridges of the Pigeon river basin and about 200mm (~ 8 in) over

the south and east facing ridges, with witness reports of a large flash-flood at 00:05 UTC on August 27th in the town of Clyde¹. The rainfall threshold for landslide and debris flows based on the historical record is 125 mm over a 24 hour period (Witt, 2005). The groundwater table rose by about 0.75m during Fay, according to the only USGS monitoring well located in Haywood County (HW-047). This is indicative of the strength for surface-groundwater interactions in the basin, despite its location on the Blue Ridge physiographic province (Brahana et al. 1986).

3. Model and Data description

3.1 Three-Dimensional Land Surface Hydrology Model (3D-LSHM)

A fully-distributed and physically-based hydrologic model, the 3D-LSHM, is used in this research. The 3D-LSHM was originally developed as column model for investigating land-atmosphere interactions (Barros, 1995), and has evolved over the years into a distributed hydrologic model solving the coupled water and energy balance equations including coupled surface-subsurface interactions (Devonec and Barros, 2002; Yildiz, 2001; Yildiz and Barros, 2005 and 2007; Yildiz and Barros, 2009). The 3D-LSHM consists of three coupled modules: a vertical Land Surface Hydrology Model (LSHM), a two-dimensional Surface Flow Routing Model (SFRM), and a two-dimensional Lateral Subsurface Flow Routing Model (LSFRM). There is no interaction between the local and regional groundwater systems. At each location, the vertical soil column consists of both an unsaturated zone and a conditionally saturated zone. The unsaturated zone is discretized into three layers, of which the 1st layer is the superficial soil zone at the land-atmosphere interface, the 2nd and 3rd layers are root layers. Overland flow is

¹ <http://www4.ncdc.noaa.gov/cgi-win/wwcgi.dll?wwevent~ShowEvent~727000>

estimated either from rainfall excess (Horton) mechanism or saturation excess (Dunne) mechanism for each grid element at each time step and routed by the SFRM, which relies on a one-dimensional kinematic wave approximation along the down-slope direction, assuming a linear flow surface across grid cells (Yildiz and Barros, 2007). The Muskingum-Cunge method of variable parameters (Ponce and Yevjevich, 1978) is utilized for the channel routing without significant backwater effects. Subsurface flow, comprising interflow and baseflow, is then laterally routed by the LSFRM. A multi-cell approach (Bear, 1979) is adopted and modified for subsurface flow routing. A more detailed description of the model can be found in (Yildiz, 2001; Devonec and Barros, 2002; Yildiz and Barros, 2005, 2007 and 2009).

3.2 Meteorological forcing data and other auxiliary data

The Digital Elevation Model (DEM) was obtained from the National Elevation Dataset (NED) at 3arcsec resolution and subsequently averaged to match model resolution (250 m). Soil parameters (i.e. saturated hydraulic conductivity K_{sat} , porosity ϕ , field capacity θ_{fc} and wilting point θ_{wp}) were extracted from the STATSGO database. The extracted soil surface texture map (Figure 2) indicates that the dominant soils over the three headwater catchments are gravelly loam, sandy loam, fine sandy loam and moderately permeable loam. The minimum value of vertical saturated hydraulic conductivity of the top 10 standard soil layers in STATSGO is used for aggregated soil layers assuming the layer with minimum hydraulic conductivity controls the time-scale of overall hydrological response. The predominant values of other soil properties, such as porosity, field capacity and wilting point, were used for the multiple soil layers. Leaf Area Index (LAI) and albedo were generated from MODIS MCD15A2² and MCD43B3³

² MODIS/Terra+Aqua Leaf Area Index/FPAR 8-Day L4 Global 1km SIN Grid V005

³ MODIS/Terra+Aqua Albedo 16-Day L3 Global 1km SIN Grid V005

products respectively. Fractional vegetation cover was estimated from LAI, based on an empirical relationship (Choudhury, 1987; French et al., 2003).

Meteorological forcing data were extracted and downscaled from NCEP North American Regional Reanalysis (NARR) (Mesinger et al., 2006), including air temperature, air pressure, wind velocity, radiation, and specific humidity. NARR fields of forcing variables are available at 32-km spatial resolution and 3-hour temporal resolution. The nearest-neighbor method was utilized to interpolate NARR fields to higher spatial resolution, and linear interpolation was applied to interpolate in time. Other parameters were specified based on personal inspection and a survey of the literature and prior studies in the Appalachians (Campbell, 1974; Chow, 1959; Clapp and Hornberger, 1978; Dickinson et al., 1993; Jackson, 1981; Price et al., 2010 and 2011; Yildiz and Barros, 2005, 2007, and 2009).

4. Rainfall Datasets

4.1 Raingauge Observations

Hourly rainfall measurements were assembled from three categories of raingauge observations. The first is the high-quality controlled rainfall dataset from the 1st phase of the Precipitation Measuring Mission (PMM) rain-gauge network in the Great Smoky Mountains (GSMRGN). GSMRGN gauges were installed at mid to high elevations (ranging from 1150m to 1920m) along exposed ridges in the Southern Appalachians (Figure 1), where no antecedent raingauge measurements were obtained before the summer of 2007, and includes 32 tipping bucket raingauge locations (Prat and Barros, 2010a). At the time of Tropical Storm Fay, 20 raingauges were in operation. The second and third datasets were obtained from the Environment and Climate Observing Network (ECONet) and Hydrometeorology Automated Data System

(HADS), respectively. HADS precipitation datasets are one of the major sources of raingauge observations used to derive the multi-sensor QPE fields (Kim et al., 2009; Nelson et al., 2010; Seo, 1998b; Seo and Breidenbach, 2002), and will be used together with other rain-gauge observations in this study to adjust QPE in the Pigeon river basin. Both ECONet and HADS are installed at low elevations or in valleys and thus augment the PMM GSMRGN data as illustrated in Figure 1. Locations and elevations of GSMRGN, ECONet and HADS raingauges referenced in this study are shown in Table 1.

4.2 The Next-generation QPE products (Q2)

The National Mosaic and Multi-sensor QPE (NMQ) project at the National Oceanic and Atmospheric Administration (NOAA) National Severe Storms Laboratory (NSSL) operationally provide the Next Generation Multi-sensor QPE (Q2) that encompasses hourly radar-based and gauge-adjusted rainfall fields at high spatial resolution ($1\times 1\text{km}^2$) (Vasiloff et al., 2007). Vasiloff (2009) reported that Q2 data tend to underestimate rainfall significantly for convective storms. Factors responsible for the underestimation include strong winds, the vertical reflectivity gradient of radar, radar scan over-shooting problems, and the radar retrieval algorithm. In regions of complex terrain such as the region of this study, the Q2 product reflects the scarcity raingauge observations. In this study, hourly radar-based and local gauge-corrected Hybrid Scan Reflectivity (HSR) products (Q2RAD_HSR_GC) were obtained from NSSL, and further adjusted using the raingauge observations from GSMRGN, as well as ECONet and HADS.

4.2.1 Assessing Q2 products based on gauge observations

To evaluate Q2 products, hourly radar-based and gauged-corrected rainfall accumulation products Q2RAD_HSR_GC (Q2 in short) were compared to rain-gauge observations over Haywood County from Aug.25 to Aug.28, 2008. The comparisons of Q2 data ($1\times 1\text{km}^2$) with

raingauge observations are shown in Figure 3a, in terms of both accumulation (mm) and rainfall intensity (mm/hr) during the storm event. Figure 3a.1) shows that the cumulative precipitation totals from Q2 are at least 50% below raingauge observations. Note the large spatial variability of rainfall as indicated by the spread of gauge rainfall traces. Q2 underestimates rainfall rate significantly, not surprisingly due to the lack of reliable NEXRAD observations in the area, especially for the very heavy rainfall events (rainfall rate > 20 mm/hr, Figure 3a.2). In addition, Q2 also misses many occurrences of light precipitation (<5mm/hr), as shown by the symbols on or very near the x-axis. This behavior is consistent throughout the year (not shown). Table 2 summarizes the root mean square error (RMSE) computed from Q2 and hourly rainfall rate observed by raingauges. The overall Q2 RMSE is as large as 2.18 mm/hr.

The inaccuracies of spatial QPE originate from two sources. First, large errors in rainfall estimates are attributed to systematic noise of WSR-88D as well as the local problems due to terrain complexity (e.g. the over-shooting or beam blockage) (Smith et al., 1996; Young et al., 1999). Secondly, the Z-R algorithm that converts WSR-88D reflectivity factor measurements to rainfall rate is subject to inaccuracy (Pratt and Barros, 2009; Fulton et al., 1998). Q2 is obtained through systematic bias correction and local gauge correction using HADS observations (Seo, 1998a; 1998b; Smith and Krajewski, 1991). Nevertheless, spatial variability and change in rainfall intensity associated with orographic modulation of the vertical structure of clouds and rainfall over mountainous regions can only be marginally captured by Q2, which is the reason why the RMSE computed from HADS is still very large for this particular storm, as shown in Table 2. Here, two simple methods regression based methods are employed to improve the Q2 accuracy particularly for Tropical Storm Fay taking advantage of the high-density rain-gauge network in the Pigeon river basin.

4.2.2 Adjustment of Q2 based on gauge observations

1) Linear regression (LR) adjustment

Linear regression of hourly raingauge observations and Q2 data results can be expressed in terms of the regression relationship,

$$R_g^t(i_g, j_g) = \kappa R_r^t(i_g, j_g) + \varepsilon \quad (1)$$

where R_g^t represent the raingauge measurements at time step t , and R_r^t represents Q2 rainfall at the pixels (i_g, j_g) corresponding to raingauge locations at the same time step. Subsequently, the resultant regression relationship was applied to Q2 data retrospectively over the whole area,

$$R_*^t(i, j) = \kappa R_r^t(i, j) + \varepsilon \quad (2)$$

where $R_*^t(i, j)$ is the adjusted Q2 rainfall over the area at time step t . In the case where no rainfall is observed by raingauges but rainfall is present in Q2, which could be explained by instances of hail or associated with very light rainfall (less than the minimum tipping amount of raingauge 0.253mm), $R_*^t(i, j)$ matches $R_r^t(i, j)$. For the case when rain gauges detect rainfall but null-rainfall is observed by Q2 over the basin, or Q2 data are missing at that time, $R_*^t(i, j)$ is replaced with the areal rainfall derived from rain-gauge observations by inverse distance weighted (IDW) interpolation. Although this simple LR method improves the accuracy of Q2 in terms of both precipitation rate and accumulation, there is an implicit assumption of spatial stationarity that will be addressed later.

The comparisons between rain-gauge observations and the adjusted Q2 data using the LR method (Q2+_All hereafter, 'All' indicates all the gauges) are shown in Figure 3b. The

computed RMSE is reported in Table 2. This adjustment proves to be effective in adjusting the rainfall rates as compared to Q2, yielding a much lower overall RMSE (1.35mm/hr) and cumulative precipitation close to the raingauge observations (Figure 3b.1). However, this method neglects landform and elevation dependencies, such as ridge-valley gradients. That is, Q2+_All data are prone to potential overestimation for heavy rainfall and underestimation for light rainfall as suggested by Figure 3-b.2.

2) Moving contour-interval (MCI_LR) adjustment

Assuming that spatial variability in precipitation is dominated by orographic effects and less affected by the scale of the rain producing clouds at the spatial scale of the Pigeon river basin, the bias in rainfall estimation should therefore be strongly related to the local elevation (Prat and Barros 2010a). Based on this assumption, a moving contour-interval method is applied to account partially for the spatial non-stationarity in orographic precipitation effects. Specifically, moving contour-intervals of 500m elevation are specified between the ridges and the valleys. Only raingauges that are within a particular contour-interval will be utilized to adjust Q2 pixels in that interval. Otherwise, the adjustment procedure is similar to the LR method above. A lower threshold of 900m and an upper threshold of 1600m are defined to make sure the number of raingauges representative of valley and ridge conditions is larger than five, thus assuring that the regression equation is well-conditioned.

The comparisons between raingauge observations and this adjusted Q2 data using the moving contour-interval method (Q2+_H/L hereafter, 'H/L' indicates gauges at High and Low elevations) are shown in Figure 3c. The RMSEs are also presented in Table 2. The Q2+_H/L data are generally superior to those obtained by the LR method, especially for valley and ridge locations consistent with a much smaller RMSE for GSMRGN and HADS gauges (1.19mm/hr vs.

1.35mm/hr, and 0.93mm/hr vs. 1.44mm/hr), whereas the RMSE for low elevation stations (ECONet) is comparable to that from LR method (0.88mm/hr vs. 0.85mm/hr). The range of cumulative precipitation of Q2+_H/L is closer to that of raingauge observations in Figure 3c.1) compared to Q2+_All, with particular improvement for large accumulations.

The spatial distribution of precipitation accumulation for Fay is shown in Figure 4, including the original Q2 data and the two adjusted Q2 datasets (Q2+). Overall, the original Q2 product severely underestimates rainfall intensities and accumulation, while the Q2+ datasets show much higher accumulations especially at higher elevations. In particular, Q2+_H/L demonstrate slightly better spatial variability than Q2+_All, indicated by stronger ridge-valley gradients. The hourly adjustment ensures a dynamic correction of the Q2 rainfall fields halving the overall RMSE to 1.35mm/hr and 1.13mm/hr for Q2+_All and Q2+_H/L respectively. The Q2+ datasets are considered hereafter as the reference rainfall for this study, that is the best estimates of the true rainfall.

4.3 The NDFD QPF products

4.3.1 QPF performance for Tropical Storm Fay

The National Digital Forecast Database (NDFD) of the National Weather Service (NWS) provides the expected quantitative precipitation forecast (QPF) at 5×5 km² resolution accumulated during each six-hour period. QPF is first created by Weather Forecast Offices (WFOs) nationwide based on guidance from NCEP's Hydrometeorological Prediction Center (HPC), and subsequently further updated by the WFOs according to real-time hydrometeorological observations or new model guidance received, and finally forwarded and incorporated into NDFD (National Weather Service, 1999). QPF for six-hour accumulations

beginning and ending at 00:00, 06:00, 12:00 and 18:00 were obtained from NDFD⁴ for Tropical Storm Fay. Note that the local WFOs across the country update forecasts at different scheduled times, and the NDFD mosaics and merges forecasts from all WFOs every hour to incorporate new updates nationwide. Thus, even though the QPF guidance from the WFOs is not updated hourly (for example, NWS Eastern Region WFOs generally update forecasts every three hours), the NDFD provides hourly updates of the six-hour QPF products. For extreme weather events (e.g. Tropical Storm Fay), the WFOs update QPF more frequently and thus the six-hour QPF can change in an hourly basis, whereas that might be different for a moderate event. As time evolves, the QPF for the same six-hourly period can increase dramatically as more observations become available.

Spatial QPFs over the Southern Appalachians for a six-hour period (12:00~18:00 UTC on August 26, 2008) are shown in Figure 5 for 6, 3 and one-hour lead-times. The meteorological observations or new model guidance received at 09:00am at the local WFO might show very high probability of occurrence of convection, thus forecasters updated the rainfall forecast amount for the 12:00~18:00 interval to nearly twice the magnitude of the previous QPF. As the NDFD is updated hourly, though not uniformly so around the country, the 1-hour lead-time QPF should be the most accurate prediction. A series of QPFs with one-hour lead time on Aug. 26 and 27 are shown in Figure 6 to illustrate the best predictions of Fay's evolution over the region. The 1-hour lead-time QPF suggests that convection would be present in the region of study between 12:00~18:00 on Aug. 26, and then move northeastward. The spatial QPF patterns show that the heaviest rainfall was forecast over the eastern ridges of the Southern Appalachians spanning the WFPRB and the EFPRB.

⁴ <http://has.ncdc.noaa.gov/pls/plhas/HAS.FileAppSelect?datasetname=9959>

4.3.2 Assessing NDFD QPF products

Evaluation or verification of QPF is a challenging proposition. Many verification methods have been proposed to assess spatial QPF in terms of rainfall intensity errors, structure errors, and skill scores such as the number of hits, misses, false alarms, and correct negatives (Gilleland et al., 2009). We will focus on assessing two essential characteristics of QPF that are of most importance for flash-flood forecasting, namely intensity magnitude and convective timing, through the comparison of QPF with raingauge observations and also QPE (both Q2 and Q2+).

To evaluate the performance of QPF for Fay with respect to the timing of heavy rainfall, that is when convective activity is present, an intercomparison between QPF and raingauge observations was conducted. The six-hour rainfall amounts observed by raingauges were first calculated, according to the same six-hour schedule as that of the NDFD QPF. Because the QPF data have coarse spatial resolution, raingauge observations within the same QPF grid were first averaged, and then compared with QPF. To compare QPF against Q2 and Q2+, the corresponding six-hour precipitation accumulations were calculated from Q2 pixels (1km) and then uniformly distributed to NDFD QPF grids (5km).

Figures 7 and 8 show the comparison between averaged six-hour rainfall amounts from the raingauges, Q2, Q2+ and the areal-averaged QPFs with six and one-hour lead times. It is clear that some updates applied to the QPF are incorrect, and thus cause underestimation or overestimation of rainfall. Nevertheless, overall, the one hour lead time QPF outperforms the six-hour lead time QPF. The scatter plot embedded in Figure 7 compares 1-hour lead time QPFs against the averaged six-hour rainfall from the gauges within the corresponding QPF grids. Note the split of the points above and below the one-to-one line and the concentration of points near the y-axis or the x-axis indicating both overestimation and underestimation at different times

reflecting temporal off-sets. Because the timing of convective cells and their spatial trajectories are very difficult to predict, it is not unexpected that the QPFs exhibit a delay or anticipation error with regard to the forecasted convection time. For example, the QPF predicts convection between 12:00~18:00 UTC on Aug.26. However, the raingauge observations indicate that most convection took place between 18:00 and midnight on Aug.26, thus an anticipation error (false alarm). The update in the 1-hour lead time QPF for 12:00~18:00 on Aug.26 (Figure 7 b) stands out due to its large overestimation of precipitation, surpassing in magnitude the six-hour lead time QPF, and also both the Q2 and Q2+ datasets. Figure 8 reveals clearly that in some other cases, the NDFD QPF underestimated precipitation severely compared to Q2 datasets, and especially with respect to the Q2+ data. Because the Q2 and Q2+ data sets are not affected by the QPF convection timing error discussed earlier, the one-hour lead time QPF overestimation error is therefore a timing error.

Furthermore, the QPF shows consistently larger rainfall than Q2 especially after the storm peak (within 18:00 on 26 ~ 00:00 on 27 Aug.) is reached as indicated by larger black bars versus blue bars in Figure 7. Interestingly, even though QPF underestimates rainfall compared to the near-truth rainfall observations (Q2+) and does not capture Fay's space-time variability, it is closer to Q2+ than Q2. This is a positive sign as it indicates that the NWP forecasts upon which QPF is based describe the temporal evolution of the storm correctly, even if they do not capture the space-time patterns correctly.

4.4 Spatial-temporal downscaling

For convective storms, the storm position within a catchment is critical to the occurrence of flooding (Moore et al., 2006). Thus a nearest-neighbor interpolation was applied to downscale rainfall fields at 1km resolution to high-resolution (250m×250m) in order to preserve the spatial

position of precipitation structures and to impose mass conservation. Then, the five-minute rainfall rates were estimated by a time-disaggregation procedure to distribute the hourly rainfall over the 12 five-minute intervals in each hour. Specifically, the 5-min rainfall intensity was generated from the Q2 datasets using $p_t = f_{i,j}P_i$, where p_t is the rainfall rate at the t^{th} time step (mm/5min), and $t = j + (i - 1) \times 12$. $f_{i,j}$ is a rainfall intensity fraction (RIF) at the j^{th} 5min of the i^{th} hour. P_i is the accumulated Q2 rainfall during the i^{th} hour (mm/hr). $f_{i,j} = p_t^g / P_i^g$ was obtained from the rain-gauge tip series, where g indicates raingauge data. Clearly, this approach could not be pursued in ungauged basins. The point here is to investigate QFF skill where data are available, so that QFF prospects in ungauged locations can be assessed.

Based on QPE (Q2) and QPF from NDFD, it is then feasible to predict streamflow in advance by forcing the 3D-LSHM with the historical, near real-time and predicted rainfall time series. To reconstruct the time-series of rainfall fields, historical and real-time QPE were derived from Q2 datasets assuming that data latency (i.e. processing time required for gauge correction at NSSL) is negligible. QPF was then used beyond the current/forecasting time. The conceptual configuration of this reconstruction is shown in Figure 9. As time evolved, updated QPF was incorporated and the length of QPE forcing extended to the forecasting time. To create rainfall input for the 3D-LSHM, six-hour QPF fields were linearly interpolated into hourly rainfall rates at the spatial resolution of the original NDFD grids (5km) first, and then interpolated into rainfall rates at 1km resolution using a nearest neighbor interpolation method. Lastly, rainfall fields at 5-min and 250m resolution were generated from the reconstructed hourly rainfall data using RIF and interpolated from the 1km data resolution of Q2 using a nearest-neighbor method, as previously described.

5. Quantitative flash-Flood Estimates (QFEs) based on QPE

5.1 QFE based on Q2 and Q2+

The 3D-LSHM was used to produce deterministic Quantitative flash-Flood Estimates (QFEs) during Tropical Storm Fay over the three headwater catchments of the Pigeon River described above: the Cataloochee Creek Basin (CCB), the West Fork Pigeon River Basin (WFPRB), and the East Fork Pigeon River Basin (EFPRB). Model simulations were conducted at 250m×250m spatial resolution and 5-min timesteps for the three basins.

5.1.1 Cataloochee Creek Basin (CCB)

The CCB has a drainage area of 128km² and features a wide flat valley with deep soil and alluvial deposits. The dominant soil texture is fine sandy loam and loam (Figure 2), with large saturated hydraulic conductivity K_{sat} as 2.8×10^{-5} m/s at ridge and 0.9×10^{-5} m/s at valley, porosity ϕ ranging from 0.434 to 0.491, field capacity θ_{fc} ranging from 0.159 to 0.259 and wilting point θ_{wp} ranging from 0.081 to 0.163 (Table 3). The CCB is located in the Great Smoky Mountain National Park, covered by very dense forest (mainly deciduous forest, Figure 2) with thick and humid top soil layers (cloud immersion is frequent). The first permeable soil layer of 15cm is above a less permeable root zone comprising the 2nd and 3rd layers of 50cm and 80cm respectively. A base layer of 1m constituted by alluvial deposits lay underneath the vadose zone.

Simulated hydrographs (QFEs) by the 3D-LSHM driven by precipitation datasets (Q2 and Q2+) over CCB are shown in Figure 10a. The estimated streamflows and the flow components for the Q2+_H/L simulations are presented in Figure 10b. The performance of all simulations was assessed by estimating peak discharge, peak time, and total discharge volume errors (Table 4), as well as the relative contributions of overland flow, interflow and baseflow components to the

total discharge for each simulation. For the QFEs forced by Q2+ datasets, the peak time of the simulated hydrographs are close to the observations with timing errors as measured by the difference between actual and forecast time-to-peak as small as -0.17hr (about 10 minutes) and -0.33hr (about 20 minutes) for Q2+_All and Q2+_H/L respectively. Meanwhile, peak value errors are with 10% of the observed peak flow, especially for the QFE driven by Q2+_H/L, the peak error is less than 3%. Note that timing and peak flow errors are respectively larger and smaller for the Q2+_H/L, which suggests that the contour based regression is capturing well spatial differences in rainfall intensity fraction (RIF) but not the temporal evolution of the storm over the catchment (see also small negative bias at very high rainfall rates in Figure 3). There is also very good agreement with regard to the falling limbs of the hydrographs and overall recession curves (Figure 10a). The time delay in the rising limb is explained by imperfect initial conditions in terms of soil moisture (no observations were available, so a representative climatologic value was used), and the fact that even at the relatively high spatial resolution the stream network fails to capture the lower order streams and in particular rills and depressions where flows tend to concentrate during such extreme events. Figure 10b shows that interflow (blue line) is the dominant flow component in the CCB throughout the storm duration. Overland flow remained small until the extremely heavy rainfall occurred around midnight on Aug.26 soon after it peaked, albeit with much lower values than the interflow. The peak time of streamflow is nearly concurrent to that of interflow. In fact, as shown in Table 4, interflow contributes around 60% of the total volume of streamflow generated by the 3D-LSHM driven by the Q2+ datasets. The large interflow contribution to streamflow is consistent with the basin's geomorphology and low elevation alluvial deposits.

Note that overall volume errors are smaller in the case of Q2+_H/L rainfall forcing (0.34%, Table 4). These QPE fields explicitly incorporate the differences between ridge and valley precipitation, and therefore a more accurate description of the spatial variability of rainfall in the CCB can capture the differences between hillslope response (shallow soils, steep slopes) and valley response (deeper soils, flat slopes). Geomorphic characteristics are therefore a key control in rainfall-runoff response in the CCB. In addition, the simulation driven by Q2+_All has a smaller total volume of streamflow (indicated by negative volume errors -4.66% in Table 4), because the LR method tends to underestimate lower rainfall rates (e.g. ≤ 5 mm/hr) which are dominant over the CCB during Fay. Frequent landslide activity in the highly unstable slopes of the CCB can be traced to the combined interflow and baseflow controls of rainfall-runoff response which account for roughly 95% of the discharge.

5.1.2 West Fork Pigeon River Basin (WFPRB)

The WFPRB has a small drainage area (71km^2) and is characterized by steep and narrow stream channels. Gravelly loam dominates the high elevation ridges and sandy loam is the dominant soil type in the valley (Figure 2). Consequently, the saturated hydraulic conductivity is large over the ridges ($K_{\text{sat}} \sim 2.8 \times 10^{-5} \text{m/s}$), and smaller in the valleys ($K_{\text{sat}} \sim 0.9 \times 10^{-5} \text{m/s}$) in the valley (Table 3). Ridge soils are thin (top soil layer is about 5cm deep) and have high porosity ϕ (0.513), low field capacity θ_{fc} (0.207) and low wilting point θ_{wp} (0.093).

QFEs simulated over the WFPRB from 3D-LSHM driven by Q2 and Q2+ datasets are shown in Figure 11a. The apportionment of discharge among overland flow, interflow and baseflow is shown in Figure 11b for simulations driven by Q2+_All. As it can be seen from the figure, streamflow simulations driven by Q2+ capture the peak value, peak time and falling limb very well, showing time-to-peak error about 1% and also very small peak errors (Table 4). Due

to the thinner soils overlaying bedrock (thus less subsurface storage), substantial overland flow occurred in the presence of heavy rainfall and baseflow is very small. The sharp overland flow hydrograph is consistent with fast response in steep slopes and steep channels. Thus, overland flow makes an important contribution to peak discharge in contrast with the CCB. Note that the predominant component of streamflow over the WFPRB is still interflow, accounting for a large portion (in excess of 56%) of the total volume, whereas baseflow is very small (Table 4). The simulation driven by Q2+_All shows generally better performance than that by Q2+_H/L, and the total flow volume is very close to the observed magnitude (about 0.17% error). The precipitation gradients in the WFPRB are small and the catchment received a moderate amount of rainfall during Fay, and therefore Q2+_All is the more appropriate rainfall forcing since the adjustment represents the overall correction.

5.1.3 East Fork Pigeon River Basin (EFPRB)

The EFPRB has similar relief as the WFPRB along the ridges but is characterized by a much wider and longer central valley (Figure 1 and Figure 2). The dominant land cover is also deciduous and mixed forest, but with fractional pasture and extensively developed areas in the flatter areas of the valley (Figure 2). The higher elevations and more sparse vegetation result in much drier initial soil moisture conditions at this time of year over EFPRB (initialized as 20%, 30% and 40% for the three layers respectively). Soil properties over the EFPRB are quite similar to the WFPRB (Figure 2). The major difference between the EFPRB and the WFPRB is in the depth of the top soil layer (10cm in the EFPRB). The large K_{sat} , high porosity, thicker and drier soils explain the slower response of the hydrograph as there is significant available subsurface storage when the storm arrives.

Comparisons between simulations (QFEs) and observations over the EFPRB are provided in Figure 12a, and flow apportionment for the simulation driven by Q2+_H/L is shown in Figure 12b. The QFEs forced by Q2+ agree well with the observed hydrograph in terms of peak time, peak value and total water volume, with significant improvements in nowcasting errors using adjusted rainfall datasets (Q2+) as compared to Q2 (Table 4). Figure 12b shows that interflow is the faster and dominant contribution to streamflow regarding both flow rate and total volume. The fast timing of the interflow response reflects the contributions from the steep slopes along the ridges. However, it is the deep soils and wide valley landscape, similar to the CCB, which explain the magnitude of interflow.

In Table 4, the highlighted error metrics indicate the best performance of QFE for each term. Note that there are significant improvements in peak values and water volumes of QFEs for the three basins using Q2+ datasets compared to the QFE driven by Q2 as expected. As for the time-to-peak error, the QFEs driven by Q2+_All have the smallest errors over the CCB and EFPRB, respectively 0.17hr (about 10 minutes) and 0.58hr (about 35 minutes) at the outlet. Over the WFPRB, the time-to-peak error is on the order of one hour, and the smaller magnitude of time-to-peak error is from the QFE driven by Q2. However, the sign of the error is negative (-0.83hr) where is positive for the Q2+ QFE. This illustrates the importance of space-time organization at very small scales, and the implications of using all network raingauges to derive Q2+ as opposed to a selected number within and in close vicinity to the basin. That is, bias correction should be conducted at even finer scales. Nevertheless, positive errors are always preferable for operational flash-flooding nowcasts. It should be also stressed that the QFEs with the smallest peak value error and water volume error do not always show the best peak time, for example the QFE driven by Q2+_H/L over the EFPRB has the smallest error in peak value and also good estimation of

water volume, but it exhibits a slightly larger error in the peak time (0.67hr, about 40 min) compared to the QFE driven by Q2+_All (0.58 hr, or about 35 min). Further quantitative evaluation of the QFE performance is presented in Section 7.

5.2 Uncertainty Analysis

As stated in Section 4, the LR method can potentially overestimate heavy rainfall and underestimate light rainfall due to the assumption of spatial stationary. A number of stochastic methods based on probabilistic models have been proposed to model the temporal-spatial characteristics of rainfall fields to evaluate the impact of uncertainty in rainfall input on hydrological response (Nikolopoulos et al., 2010; Schroter et al., 2011). In our study, both of the adjustment methods (LR and MCI_LR) are based on linear regression models, which minimize the sum of the squared errors (SSE) between rain-gauge observations and radar-based rainfall fields and provide ‘best fit’ predictors over the basins, assuming that the observation errors are uncorrelated and normally distributed with mean zero and constant variances. Though the comparison results in terms of both rainfall rate and accumulation demonstrate significant improvements in Q2+ data, characteristics of the uncertainty in these rainfall datasets pertaining to how they were derived from the same baseline product (Q2) and the same observations are yet to be identified. In particular, the propagation of this uncertainty in the hydrologic model and how that translates into QFE uncertainty needs to be evaluated.

For this purpose, the uncertainty and variability of rainfall were assumed first to be normally distributed (e.g. within 95% confidence intervals of regression models) for each pixel at each hour. Second, the impacts of the uncertainty in the rainfall fields on hydrological response were evaluated through Monte Carlo simulations. Rainfall replicates were randomly sampled from the normal distribution with mean as the optimal predictor and standard deviation as one third of the

confidence interval (including 99.7% of the distribution) for each pixel at each time step. In this way, rainfall replicates account for the spatial uncertainty and variability, while maintaining the temporal structure of rainfall. The same procedure was repeated for Q2+_All and Q2+_H/L. Figure 13 shows 100 rainfall replicates sampled from the 95% confidence intervals of the regression models at the pixels with raingauges, representing the rainfall variation. The variation generated from Q2+_H/L is larger than Q2+_All for the same confidence interval because Q2+_All utilized data from all the gauges, and thus the regression models were relatively more stable compared to Q2+_H/L. These 100 rainfall replicates as well as the confidence bounds at 95%, 70% and 50% were used to force the 3D-LSHM and to evaluate the impact of rainfall uncertainty on runoff response. The resultant simulations over WFPRB and EFPRB are shown in Figure 14, as well as the estimated streamflow forced by Q2+_All or Q2+_H/L.

As it can be seen from Figure 14, the simulation ensembles (blue dash lines) over the WFPRB (upper) and the EFPRB (bottom) show small discrepancies against the simulated hydrograph forced by Q2+_All or Q2+_H/L (red lines), both of which fall within the uncertainty bounds of rainfall generated at 95%, 70% and 50% confidence intervals (CI, shaded areas). However, note the spread around peak flows and falling limbs, embedded in large shaded areas indicating wide variation in streamflow volume. That is, rainfall uncertainty effects are magnified after most of the basin is hydrologically engaged by the storm. The impacts of uncertainty in rainfall on streamflow over the EFPRB are much larger than in the WFPRB. This is attributed to the fact that no raingauge exists over the EFPRB (out of the GSMRN, HADS and ECONet networks), and thus the regression models cannot capture the actual space-time structure of rainfall.

The scatter plot of relative errors in peak flow versus the corresponding RMSE calculated from the 100 rainfall replicates are given in Figure 15. The relative errors in peak flow were calculated as $[100 \times (P_{\text{est}} - P_{\text{obs}}) / P_{\text{obs}}]$, where P_{est} is the estimated streamflow peak and P_{obs} is the observed peak flow. Because the observed streamflow records are available at 15 minute intervals, whereas the simulation timestep is 5 minutes, the simulated 5-min streamflow time-series were averaged to 15 minutes, and then smoothed using a four-step (20 minutes) window to ensure continuity. It is apparent that the RMSE from replicates corresponding to the 50% CI (yellow) are smaller than those for larger CIs of the regression models. Nevertheless, the relative errors of simulated peak associated with Q2+_H/L are much smaller (within $\pm 10\%$) than those with Q2+_All over EFPRB. The opposite is true over the WFPRB, consistent with the discussion in Section 5.1 above. Yet, there is no obvious increase in the relative errors in peak flow as the RMSE of rainfall increases. The dotted areas demonstrate that the error propagation through the hydrological model is highly non-linear. Larger ranges of RMSE for Q2+_H/L than for Q2+_All indicate larger uncertainty in the Q2+_H/L dataset (Figure 15b and 15d), which translates into relative errors in peak flow with ranges on the order of 20% for both WFPRB and EFPRB. In contrast, uncertainty in Q2+_All (Figures 15a and 15c) corresponds to relative errors within the 10% range for WFPRB (-5%~5%) and also 20% for EFPRB (0%~20%). Therefore, the propagation of rainfall uncertainty through the 3D-LSHM can be explained by basin geomorphological attributes and hydrologic conditions.

6. Quantitative flash-Flood Forecasts (QFFs) based on QPE and QPF

The success in nowcasting (QFE) streamflow response for Fay encourages the investigation of Quantitative flash-Flood Forecasts (QFFs) in the Great Smoky Mountains driven by the

combination of historical and real-time QPE and future QPF time series. Clearly, streamflow forecast skill is strongly dependent on the hydrologic model. However, as documented in Sections 4 and 5, the performance of the hydrologic model is determined to first order by the rainfall forcing. The value added by near realtime satellite-based remote sensing products into operational QPE (Q2) will also be assessed to show the possibility to obtain benefits of satellite products for flash flood forecasting.

Because of their unimpeded view of precipitation systems from the top, there has been great expectation with regard to the utility of satellite products for improving flood forecasting performance especially for fast response events and in regions of complex terrain (Collier, 2007). Here, we demonstrate the potential value of Global Precipitation Measurement (GPM) mission observations in the Southern Appalachians to improve flash flood forecasting. GPM, scheduled for launch in February 2014, will provide frequent (about every 3-6 hours overpass revisit interval) enhanced precipitation observations (Hou et al., 2008; Neeck et al., 2010; Tapiador et al., 2011). For this purpose, a simple GPM OSS (Observing System Simulator) concept that relies on the assumption that the GPM rainfall retrieval algorithms and observations would yield rainfall fields that match the Q2+ datasets at the time of overpass was implemented. Specifically, GPM proxy data were generated by sampling Q2+_All and Q2+_H/L every three hours assuming negligible error. The proxy GPM products were subsequently nudged to Q2 in real time, and the merged product is used as QPE for each forecasting time as illustrated in Figure 9.

Figure 16 shows the merged Q2 with proxy GPM over the WFPRB (a) and EFPRB (b). Consider a time sequence (SSSSSS) where S is a pixel value of Q2+ rainfall on the GPM trajectory at the time of overpass, and X is the corresponding Q2 value. The notation Q2&GPM# is intended to indicate that Q2 datasets incorporated the available GPM products

generated by sampling from Q2+ according to three sampling order denoted by #: Q2&GPM1 (green) refers to the merged (SXXSXX) sequence, Q2&GPM2 (blue) refers to (XSXXSX), and Q2&GPM3 (red) refers to (XXSXXS).

There has been extensive work on assessing satellite error metrics of satellite rainfall and its implications for real-time hydrological applications at various spatial and temporal scales (e.g. Gourley et al., 2011; Hossain and Huffman 2008; Hossain and Anagnostou, 2006; Hossain et al., 2004; Nijssen and Lettemmaier 2004; and many others). Previously, Pratt and Barros (2010b) conducted error analysis of TRMM PR (Precipitation Radar) rainfall estimates specifically focusing on Tropical Storm Fay, which could be used as a basis to derive a satellite rainfall error and bias correction models. However, here, the focus is on the importance of satellite revisit times alone, and observational errors at the time of overpass are assumed negligible for simplicity. The QPE is based on Q2 alone, because in standard operational circumstances there will not be a high density raingauge network available, and greatest value from satellite information is to be gained in ungauged basins.

Only QFF produced by the rainfall incorporated into GPM products generated from Q2+_All for WFPRB and from Q2+_H/L for EFPRB are examined next (Figures 17 and 18). In Figures 17 and 18, the point where the dashed line changes to solid line represents the forecast issue time or current time t_c . Before time t_c rainfall forcing is the QPE (Q2 without or without satellite information), and after t_c the rainfall forcing is QPF. The predicted streamflow (QFF) at time t (x-axis) has a lead time $(t-t_c)$. The predicted streamflow (QFF) at time t (x-axis) has a lead time $(t-t_c)$. The forecast hydrographs in green, blue and red represent the streamflow forecasts forced by Q2&GPM# corresponding to sampling order # as displayed in Figure 16.

Figures 17 and 18 show that the Q2-QPF driven QFFs (yellow lines) severely underestimate both the peak and volume of the river flow, even though QFFs increase somewhat at some particular forecasting times which can be attributed to the QPF overestimation discussed in Section 4.3. The lack of QFF skill documented here is not unexpected (National Research Council, 2005).

Three QFFs made at 12:00am on Aug.26 and at 00:00am on Aug.27 are shown. Figure 17 demonstrates clearly that the QFF performance in the WFPRB is significantly better with the incorporation of GPM observations, in particular note the improvement in the QFF issued at 00:00am on Aug.27. Although the satellite proxy observations cannot resolve the problem of missing rainfall as it can be seen from the difference of cumulative precipitation, the streamflow nowcast shows strong peak response, with peak flow and peak time consistent with observations. In this case, the key factor is the concurrence of the precipitation system and satellite overpass over the basin.

Unlike the significant improvements in QFF over the WFPRB, the streamflow forecasts over the EFPRB exhibit minimum improvement between the simulations with and without the GPM proxy observations (Figure 18). Because of Fay's persistent rainfall over the EFPRB (Figure 16), the instantaneous satellite observations do not add significant new information as compared to that that is available in the QPE. In addition, a very important physical control of flash flood response is missing: that is, the soil moisture condition at the forecasting time which depends on the prior rainfall-runoff response history. That is, the lack of improvement for the EFPRB with an area about twice that of the WFPRB has not to do with spatial scale per se, or with rainfall forcing alone, but with the ability to capture the space-time evolution of the dominant hydrological processes. This suggests that continuous hydrological simulation of such basins

through improving estimates of soil moisture fields at high spatial resolution for example assimilating soil moisture data would have a significant impact on assessing flash flooding potential, and on QFF skill. Nevertheless, the absolute magnitude of peak flows generated for Q2&GPM# (green, blue and red line) are more than twice the peak value of the yellow line (Q2), and have better peak timings as well, despite the severe underestimation and time delay. The QPF influences the QFF accuracy substantially. Note that the cumulative precipitation in a) at the end of simulation period is always much larger than that in b) both in Figure 17 and 18, which is attributed to the overestimation of QPF with large lead times on the one hand, and the Q2 systematic underestimation on the other (see discussion in Section 4). As time evolves, QPF is replaced by Q2 as forecasts become hindcasts, and the QFF becomes even worse for some situations. For instance the hindcast at 00:00am on Aug.29 is poorer than that at 00:00am on Aug. 27 over the EFPRB (Figure 18). By contrast, the merging of GPM proxy observations with Q2 always leads to improvements, independently of whether the overpass is concurrent with heavy rainfall or not for both WFPRB and EFPRB. Shorter satellite revisit times would lead to increasingly improved QFF, which may be achieved in the future by multiple platforms.

7. QFE and QFF Performance Metrics for Tropical Storm Fay

To evaluate the performance of both QFE and QFF quantitatively, error statistics associated with flash-flood nowcasts and forecasts are computed and compared. In this study, three error indices are used to evaluate the performance of QFE and QFF for Fay, namely Root Mean Square Error (RMSE), RMSE-observations standard deviation ratio (RSR) and Nash-Sutcliffe efficiency (NSE). The RMSE is a commonly used error index for evaluating operational flood forecasts, e.g. verification of river forecasting (Demargne et al., 2009). The RSR is a RMSE

normalized by the standard deviation of the observations (Moriasi et al., 2007). The NSE is a widely used indicator for evaluating the goodness of simulation compared to observations (Nash and Sutcliffe, 1970). These error indices are modified to account for the forecast errors with respect to variant lead times, as shown in Equations (3) to (5):

$$\text{RMSE: } e_j = \sqrt{\frac{\sum_{i=1}^N (\hat{Q}_{ij} - Q_i)^2}{N}} \quad (3)$$

$$\text{RSR: } e_j = \frac{\sqrt{\sum_{i=1}^N (\hat{Q}_{ij} - Q_i)^2}}{\sqrt{\sum_{i=1}^N (Q_i - \bar{Q})^2}} \quad (4)$$

$$\text{NSE: } e_j = 1 - \frac{\sum_{i=1}^N (\hat{Q}_{ij} - Q_i)^2}{\sum_{i=1}^N (Q_i - \bar{Q})^2} \quad (5)$$

where e_j indicates forecast error for lead time j , \hat{Q}_{ij} is the forecasted streamflow at time step i with a lead time j , while Q_i means the observation at time step i and \bar{Q} is the mean of observations. N represents the total number of observations. Both RMSE and RSR are always larger than or equal to zero, while NSE ranges from $-\infty$ to 1. The lower the RMSE and RSR, the better the forecasting performance. For the NSE, the closer the values are to unity the better the performance, and positive NSE values are indicative of useful (acceptable) performance (Moriasi et al., 2007). In the literature, error statistics are calculated typically for daily streamflows and larger basins, whereas the error metrics are calculated for each basin using 15-min time-series of both observations and forecasts as described next.

To calculate the error metrics, the estimated and forecasted 5-min streamflow time-series were averaged to the 15-minute temporal resolution of the observations as described in Section

5.2. For nowcasts, the QFF is actually a QFE at the forecasting time. Table 5 presents the summary of QFE error indices for Fay. Both RMSE and RSR with Q2+ as the rainfall forcing are reduced to less than half of the value when using Q2, especially for EFPRB. Likewise, tremendous improvements are found in the NSE values for Q2+ which become very close to 1, whereas NSE values were negative for Q2 driven QFE. Confirming earlier assertions, Q2+_All is the best dataset for WFPRB while Q2+_H/L is best for EFPRB, indicated by the highest NSE of 0.82 for the QFE forced by Q2+_All over the WFPRB, and the highest NSE of 0.90 for the QFE forced by Q2+_H/L over the EFPRB. These values are remarkable considering the time-scales of interest in this study, and confirm the high level of performance of the 3D-LSHM without calibration.

A summary of the error statistics of QFFs over the WFPRB and the EFPRB for a range of lead times are displayed in Figure 19. All error statistics become worse with increasing lead times up to six hours, which is usually taken as the upper limit of the characteristic response time of flash floods. For the WFPRB, both the RMSE and RSR are reduced while the NSE increases substantially comparing to the error indices of QFF without GPM information. It should be stressed that the NSE of the QFF generated by the 3D-LSHM driven by Q2&GPM2 (Q2+_All)_QPF is actually positive, though small, thus implying that the forecast skill is useful. In contrast to the WFPRB, all the QFF error statistics only improve marginally over the EFPRB with GPM as expected from the analysis in Section 6. In addition, error metrics do not change significantly with increasing lead time, which means that the overall forecast skill is poor.

Overall, the results for the two Q2+ datasets are consistent with the conclusions in Sections 4 and 5. The difference between the two different revisiting times (GPM2 vs. GPM3) for these two adjacent catchments shows that the ability to capture large rainfall variability both in space

and time is essential for producing accurate unbiased QFF, and that increased overpass frequency should lead to improved forecasts. Due to the multi-satellite, multi-sensor architecture of GPM, and the increasing number of active geostationary weather satellites, there is great potential to engineer higher frequency rainfall observing schemes over regions of the world with higher overpass density (Hou et al. 2008).

8. Summary and Discussion

A detailed investigation of the relationship between space-time variability of rainfall and flashflood forecasting in regions of complex topography was conducted using a high-resolution physically-based hydrological model (3D-LSHM) driven by operational QPE and QPF for Tropical Storm Fay. The operational QPE product Q2 was adjusted based on error structures derived from the comparison between rain-gauge network observations and hourly Q2 rainfall fields. The adjusted rainfall datasets (Q2+) show significant improvement, with remarkable reduction in the RMSE of hourly rainfall, especially when the ridge–valley rainfall gradients that result from linear orographic effects were taken into consideration.

The QFEs produced by the 3D-LSHM driven by Q2+ rainfall fields over three small headwater catchments of the Pigeon River in the Southern Appalachians agree well with observations in terms of both peak characteristics and total flow volume with NSE values close to 0.9, which indicates that flash floods are predictable using the uncalibrated model given reasonable rainfall forcing. Furthermore, we show that a critical factor of predictability is the model's ability to capture the interflow regimes of the different basins. This is consistent with Flugel and Smith (1999) who argued that interflow is the dominant rainfall-runoff response process in headwater catchments. Two geomorphic traits are favorable for the generation of

significant interflow: deep soils in flat and wide valleys (e.g. CCB and EFPRB), and thin soils in very steep slopes and narrow valleys (e.g. WFPRB). Though the generation mechanism is different depending on basin hydro-geomorphic properties, the contribution of interflow to total discharge was dominant (50%~70%), with higher values for the CCB. It is therefore critical to correctly estimate flow components of streamflow not only river discharge, as different water pathways are linked to other hydrometeorological mountain hazards, e.g. debris flows, mudflows and landslides (Witt, 2005; Wooten et al., 2008; Liao et al. 2011). This is particularly important in the case of long-duration regional-scale events such as tropical storms and hurricanes that engage multiple basins and different sectors of the same basin at different times.

Propagation of space-time uncertainty in rainfall to streamflow estimation by the hydrologic model was assessed through Monte Carlo simulations. The results show that the propagation of uncertainty in rainfall through the hydrological model is highly non-linear, and depends on basin hydro-geomorphology and the evolution of soil moisture conditions with time. Figures 20a and 20b show rainfall and soil moisture fields in the top three layers corresponding to the 70% CI bounds and ensemble mean for the Monte Carlo simulations over the EFPRB at two selected times (see Figure 14). Note the uncertainty in the spatial distribution of soil moisture, the gradients of which reflect the spatial organization of large interflow that in turn can trigger landslides. This illustrates the importance of distributed hydrologic modeling for a comprehensive assessment of natural hazards in mountainous regions.

Deterministic operational QFFs during the passage of Tropical Storm Fay over the Pigeon River basin were simulated using Q2 QPE and NDFD QPF to examine QFF performance in the WFPRB and the EFPRB. The utility of introducing satellite rainfall observations into QPE for improving flash flood forecasting was subsequently evaluated by merging GPM-like rainfall

fields with Q2 at scheduled overpass times. The results show that significant improvements estimated from ground-based radar can improve the accuracy of QFF significantly for the WFPRB. Even when the three-hour revisit times are such that the peak rainfall periods are missed, the forecasts still represent an improvement over current guidance. This was not the case for the EFPRB, in which case the evolution of soil moisture conditions across the basin during the actual event is critical to determine the timing of flash flood response. Thus, the improvement depends strongly on storm-dependent and basin-specific rainfall-runoff dynamics suggesting that a continuous simulation approach in contrast to the threshold based approach that is often used in operational Flash Flood Guidance.

Whereas the current study was conducted with the access to a high density, science-grade raingauge network over the region, the QFF demonstration is illustrative of expected performance in ungauged basins. As suggested by previous studies, approaches to improve QPF through post-processing using for example artificial neural networks (ANN) and Model Output Statistics (MOS) (Kuligowski and Barros, 1998a and 1998b). Kim and Barros (2001) showed that far- range satellite-based observations [both rainfall and storm structure] could be used along with remote ground-based information [profilers and raingauges] in data-driven models (ANN specifically) to improve the skill and lead-times (18-24 hours) of flood forecasts in the Northern Appalachian Mountains, albeit for larger basins [750 - ~9,000 km²]. These approaches indicate that a global-scale warning and emergency response system of hydrometeorological hazards (e.g. Hong et al. 2007; Hossain 2006) is within reach as access to multisensor satellite observations including rainfall (GPM), storm structure (GPM and JPSS- Joint Polar satellite System, <http://www.nesdis.noaa.gov/jpss/>), and soil moisture [e.g. SMAP- Soil Moisture Active Passive mission, <http://cce.nasa.gov/pdfs/SMAP.pdf>] on the one hand, and high-resolution QPF from

numerical weather prediction models (e.g. Sun and Barros 2012), and high-resolution QFF from uncalibrated distributed hydrologic models with data assimilation are less and less constrained by computational resources. [For example, a parallelized implementation of the 3D-LSHM can conduct concurrent simulations for various watersheds such as those described here with latencies of minutes.]

Acknowledgements

This research was supported in part by a NASA Earth System Science Fellowship with the first author, and NASA Grant NNX1010H66G and NOAA Grant NA08OAR4310701 with the second author. We are grateful to Laurence Lee of the National Weather Service, Greer South Carolina for his help and insight.

References

- Allison, J.B., Hale, L.B., Evans, S.T., 1997. Soil survey of Haywood County area, North Carolina. [Washington, D.C.]: Natural Resources Conservation Service.
- Ashley, S.T., Ashley, W.S., 2008. Flood fatalities in the United States. *Journal of Applied Meteorology and Climatology*, 47(3): 805-818.
- Barros, A.P., 1995. Adaptive Multilevel Modeling of Land-Atmosphere Interactions. *Journal of Climate*, 8(9): 2144-2160.
- Barros, A.P., 2012. Orographic Precipitation, Freshwater Resources, and Climate Vulnerabilities in Mountainous Regions. In: Pielke, R. (Ed.), *Climate Vulnerability*. Elsevier.
- Barros, A.P., Lettenmaier, D.P., 1993. Dynamic modeling of the spatial distribution of precipitation in remote mountainous areas. *Monthly Weather Review*, 121(4): 1195-1214.

- Bear, J., 1979. *Hydraulics of groundwater*. New York : McGraw-Hill Book Co.
- Bindlish, R., Barros, A.P., 2002. Subpixel variability of remotely sensed soil moisture: An inter-comparison study of SAR and ESTAR. *IEEE Transactions on Geoscience and Remote Sensing*, 40(2): 326-337.
- Borga, M., Tonelli, F., 2000. Adjustment of range-dependent bias in radar rainfall estimates. *Physics and Chemistry of the Earth Part B-Hydrology Oceans and Atmosphere*, 25(10-12): 909-914.
- Brahana, J.V., Mulderink, D., Macy, J.A., Bradley, M.W., 1986. Preliminary delineation and description of the regional aquifers of Tennessee-The East Tennessee aquifer system, U.S. Geological Survey Water-Resources Investigations Report 82-4091, Nashville, Tennessee, USA.
- Campbell, G.S., 1974. A simple method for determining unsaturated conductivity from moisture retention data. *Soil Science*, 117(6): 311-314.
- Carpenter, T.M., Georgakakos, K.P., 2006. Intercomparison of lumped versus distributed hydrologic model ensemble simulations on operational forecast scales. *Journal of Hydrology*, 329(1-2): 174-185.
- Choudhury, B.J., 1987. Relationships between vegetation indices, radiation absorption, and net photosynthesis evaluated by a sensitivity analysis. *Remote Sensing of Environment*, 22(2): 209-233.
- Chow, V.T., 1959. *Open-Channel Hydraulics*. McGraw-Hill Companies.
- Clapp, R.B., Hornberger, G.M., 1978. Empirical equations for some soil hydraulic properties. *Water Resources Research*, 14(4): 601-604.

- Collier, C.G., 2007. Flash flood forecasting: What are the limits of predictability? *Quarterly Journal of the Royal Meteorological Society*, 133(622): 3-23.
- Demargne, J. et al., 2009. Application of Forecast Verification Science to Operational River Forecasting in the US National Weather Service. *Bulletin of the American Meteorological Society*, 90(6): 779-784.
- Devonec, E., Barros, A.P., 2002. Exploring the transferability of a land-surface hydrology model. *Journal of Hydrology*, 265(1-4): 258-282.
- Dickinson, R.E., Henderson-Sellers, A., Kennedy, P.J., 1993. Biosphere-Atmosphere Transfer Scheme (BATS) Version 1e as Coupled to the NCAR Community Climate Model. NCAR Technical Note: NCAR/TN-387+STR.
- Ebert, E.E., Janowiak, J.E., Kidd, C., 2007. Comparison of near-real-time precipitation estimates from satellite observations and numerical models. *Bulletin of the American Meteorological Society*, 88(1): 47-64.
- Ebert, E.E., McBride, J.L., 2000. Verification of precipitation in weather systems: determination of systematic errors. *Journal of Hydrology*, 239(1-4): 179-202.
- Flugel, W.A., Smith, R.E., 1999. Integrated process studies and modelling simulations of hillslope hydrology and interflow dynamics using the HILLS model. *Environmental Modelling & Software*, 14(2-3): 153-160.
- French, A.N., Schmugge, T.J., Kustas, W.P., Brubaker, K.L., Prueger, J., 2003. Surface energy fluxes over El Reno, Oklahoma, using high-resolution remotely sensed data. *Water Resources Research*, 39(6).
- French, J., Ing, R., Vonallmen, S., Wood, R., 1983. Mortality from flash floods: a review of national weather service reports, 1969-81. *Public Health Reports*, 98(6): 584-588.

- Fulton, R.A., Breidenbach, J.P., Seo, D.J., Miller, D.A., O'Bannon, T., 1998. The WSR-88D rainfall algorithm. *Weather and Forecasting*, 13(2): 377-395.
- Georgakakos, K.P., Hudlow, M.D., 1984. Quantitative Precipitation Forecast Techniques for Use in Hydrologic Forecasting. *Bulletin of the American Meteorological Society*, 65(11): 1186-1200.
- Gilleland, E., Ahijevych, D., Brown, B.G., Casati, B., Ebert, E.E., 2009. Intercomparison of Spatial Forecast Verification Methods. *Weather and Forecasting*, 24(5): 1416-1430.
- Gourley, J.J., Erlingis, J.M., Hong, Y., Wells, E.B., 2012. Evaluation of Tools Used for Monitoring and Forecasting Flash Floods in the United States. *Weather and Forecasting*, 27(1): 158-173.
- Gourley, J.J. et al., 2011. Hydrologic Evaluation of Rainfall Estimates from Radar, Satellite, Gauge, and Combinations on Ft. Cobb Basin, Oklahoma. *Journal of Hydrometeorology*, 12(5): 973-988.
- Hong, Y., Adler, R.F., Hossain, F., Curtis, S., Huffman, G.J., 2007. A first approach to global runoff simulation using satellite rainfall estimation. *Water Resources Research*, 43(8).
- Hossain, F., Anagnostou, E.N., 2004. Assessment of current passive-microwave- and infrared-based satellite rainfall remote sensing for flood prediction. *Journal of Geophysical Research-Atmospheres*, 109(D7).
- Hossain, F., Anagnostou, E.N., 2006. A two-dimensional satellite rainfall error model. *Ieee Transactions on Geoscience and Remote Sensing*, 44(6): 1511-1522.
- Hossain, F., Anagnostou, E.N., Dinku, T., 2004. Sensitivity analyses of satellite rainfall retrieval and sampling error on flood prediction uncertainty. *Ieee Transactions on Geoscience and Remote Sensing*, 42(1): 130-139.

- Hossain, F., Huffman, G.J., 2008. Investigating error metrics for satellite rainfall data at hydrologically relevant scales. *Journal of Hydrometeorology*, 9(3): 563-575.
- Hou, A., Kummerow, C., Skofronick-Jackson, G., Shepherd, J.M., 2008. Global Precipitation Measurement. In: Michaelides, S. (Ed.), *Precipitation: Advances in Measurement, Estimation and Prediction*. Springer, Springer-Verlag Berlin Heidelberg, pp. 131-170.
- Huffman, G.J. et al., 2007. The TRMM multisatellite precipitation analysis (TMPA): Quasi-global, multiyear, combined-sensor precipitation estimates at fine scales. *Journal of Hydrometeorology*, 8(1): 38-55.
- Jackson, P.S., 1981. On the displacement height in the logarithmic velocity profile. *Journal of Fluid Mechanics*, 111(OCT): 15-25.
- Kelsch, M., 2002. Comet((R)) flash flood cases: Summary of characteristics. 16th Conference on Hydrology: 42-46.
- Kim, D., Nelson, B., Seo, D.J., 2009. Characteristics of Reprocessed Hydrometeorological Automated Data System (HADS) Hourly Precipitation Data. *Weather and Forecasting*, 24(5): 1287-1296.
- Kirschbaum, D.B. et al., 2011. Advances in landslide nowcasting: evaluation of a global and regional modeling approach. *Environmental Earth Sciences*: 1-14.
- Kuligowski, R.J., Barros, A.P., 1998a. Experiments in short-term precipitation forecasting using artificial neural networks. *Monthly Weather Review*, 126(2): 470-482.
- Kuligowski, R.J., Barros, A.P., 1998b. Localized precipitation forecasts from a numerical weather prediction model using artificial neural networks. *Weather and Forecasting*, 13(4): 1194-1204.

- Liao, Z. et al., 2011. Evaluation of TRIGRS (transient rainfall infiltration and grid-based regional slope-stability analysis)'s predictive skill for hurricane-triggered landslides: a case study in Macon County, North Carolina. *Natural Hazards*, 58(1): 325-339.
- Looper, J.P., Vieux, B.E., Moreno, M.A., 2012. Assessing the impacts of precipitation bias on distributed hydrologic model calibration and prediction accuracy. *Journal of Hydrology*, 418: 110-122.
- Mesinger, F. et al., 2006. North American regional reanalysis. *Bulletin of the American Meteorological Society*, 87(3): 343-360.
- Moore, R.J., Cole, S.J., Bell, V.A., Jones, D.A., 2006. Issues in flood forecasting: ungauged basins, extreme floods and uncertainty. *Frontiers in Flood Research*, 305: 103-122.
- Moriasi, D.N. et al., 2007. Model evaluation guidelines for systematic quantification of accuracy in watershed simulations. *Transactions of the Asabe*, 50(3): 885-900.
- Nash, J.E., Sutcliffe, J.V., 1970. River flow forecasting through conceptual models part I — A discussion of principles. *Journal of Hydrology*, 10(3): 282-290.
- National Research Council, 2005. *Flash Flood Forecasting Over Complex Terrain: With an Assessment of the Sulphur Mountain NEXRAD in Southern California*. National Academies Press, Washington, D.C.
- National Weather Service, 1999. *Quantitative Precipitation Forecast Process Assessment*, National Weather Service, NOAA, U.S. Department of Commerce, Silver Spring, MD 20910.
- Neeck, S.P., Kakar, R.K., Azarbarzin, A.A., Hou, A.Y., 2010. Global Precipitation Measurement (GPM) Implementation, Conference on Sensors, Systems, and Next-Generation Satellites XIV, Toulouse, FRANCE.

- Nelson, B.R., Seo, D.J., Kim, D., 2010. Multisensor Precipitation Reanalysis. *Journal of Hydrometeorology*, 11(3): 666-682.
- Nijssen, B., Lettenmaier, D.P., 2004. Effect of precipitation sampling error on simulated hydrological fluxes and states: Anticipating the Global Precipitation Measurement satellites. *Journal of Geophysical Research-Atmospheres*, 109(D2): 15.
- Nikolopoulos, E.I., Anagnostou, E.N., Hossain, F., Gebremichael, M., Borga, M., 2010. Understanding the Scale Relationships of Uncertainty Propagation of Satellite Rainfall through a Distributed Hydrologic Model. *Journal of Hydrometeorology*, 11(2): 520-532.
- NWS, 2010. <http://www.srh.noaa.gov/mrx/hydro/flooddef.php>.
- Olson, D.A., Junker, N.W., Korty, B., 1995. Evaluation of 33 Years of Quantitative Precipitation Forecasting at the NMC. *Weather and Forecasting*, 10(3): 498-511.
- Ponce, V.M., Yevjevich, V., 1978. Muskingum-Cunge Method with Variable Parameters. *Journal of the Hydraulics Division-Asce*, 104(12): 1663-1667.
- Prat, O.P., Barros, A.P., 2010a. Ground observations to characterize the spatial gradients and vertical structure of orographic precipitation - Experiments in the inner region of the Great Smoky Mountains. *Journal of Hydrology*, 391(1-2): 143-158.
- Prat, O.P., Barros, A.P., 2010b. Assessing satellite-based precipitation estimates in the Southern Appalachian mountains using rain gauges and TRMM PR. *Advances in Geosciences*, 25: 143-153.
- Price, K., Jackson, C.R., Parker, A.J., 2010. Variation of surficial soil hydraulic properties across land uses in the southern Blue Ridge Mountains, North Carolina, USA. *Journal of Hydrology*, 383(3-4): 256-268.

- Price, K. et al., 2011. Effects of watershed land use and geomorphology on stream low flows during severe drought conditions in the southern Blue Ridge Mountains, Georgia and North Carolina, United States. *Water Resources Research*, 47.
- Reed, S., Schaake, J., Zhang, Z., 2007. A distributed hydrologic model and threshold frequency-based method for flash flood forecasting at ungauged locations. *Journal of Hydrology*, 337(3-4): 402-420.
- Rosenfeld, D., Wolff, D.B., Amitai, E., 1994. The Window Probability Matching Method for Rainfall Measurements with Radar. *Journal of Applied Meteorology*, 33(6): 682-693.
- Rosenfeld, D., Wolff, D.B., Atlas, D., 1993. General Probability-matched Relations between Radar Reflectivity and Rain Rate. 32(1): 50-72.
- Schroter, K., Llort, X., Velasco-Forero, C., Ostrowski, M., Sempere-Torres, D., 2011. Implications of radar rainfall estimates uncertainty on distributed hydrological model predictions. *Atmospheric Research*, 100(2-3): 237-245.
- Seo, D.J., 1998a. Real-time estimation of rainfall fields using radar rainfall and rain gage data. *Journal of Hydrology*, 208(1-2): 37-52.
- Seo, D.J., 1998b. Real-time estimation of rainfall fields using rain gage data under fractional coverage conditions. *Journal of Hydrology*, 208(1-2): 25-36.
- Seo, D.J., Breidenbach, J., Fulton, R., Miller, D., O'Bannon, T., 2000. Real-time adjustment of range-dependent biases in WSR-88D rainfall estimates due to nonuniform vertical profile of reflectivity. *Journal of Hydrometeorology*, 1(3): 222-240.
- Seo, D.J., Breidenbach, J.P., 2002. Real-time correction of spatially nonuniform bias in radar rainfall data using rain gauge measurements. *Journal of Hydrometeorology*, 3(2): 93-111.

- Seo, D.J., Breidenbach, J.P., Johnson, E.R., 1999. Real-time estimation of mean field bias in radar rainfall data. *Journal of Hydrology*, 223(3-4): 131-147.
- Seo, D.J., Smith, J.A., 1992. Radar-based short-term rainfall prediction. 131(1-4): 341-367.
- Smith, J.A., Krajewski, W.F., 1991. Estimation of the Mean Field Bias of Radar Rainfall Estimates. *Journal of Applied Meteorology*, 30(4): 397-412.
- Smith, J.A., Seo, D.J., Baek, M.L., Hudlow, M.D., 1996. An intercomparison study of NEXRAD precipitation estimates. *Water Resources Research*, 32(7): 2035-2045.
- Smith, M.B. et al., 2012. Results of the DMIP 2 Oklahoma experiments. *Journal of Hydrology*, 418-419: 17-48.
- Steiner, M., Smith, J.A., Burges, S.J., Alonso, C.V., Darden, R.W., 1999. Effect of bias adjustment and rain gauge data quality control on radar rainfall estimation. *Water Resources Research*, 35(8): 2487-2503.
- Sun, X., Barros, A.P., 2012. The impact of forcing dataset on the high resolution simulation of Tropical Storm Ivan (2004) in the Southern Appalachians. *Monthly Weather Review*.
- Tao, K., Barros, A.P., 2010. Using Fractal Downscaling of Satellite Precipitation Products for Hydrometeorological Applications. *Journal of Atmospheric and Oceanic Technology*, 27(3): 409-427.
- Tapiador, F.J. et al., 2011. Precipitation estimates for hydroelectricity. *Energy & Environmental Science*, 4(11): 4435-4448.
- Tapiador, F.J. et al., 2012. Global precipitation measurement: Methods, datasets and applications. *Atmospheric Research*, 104: 70-97.

- Vasiloff, S.V., Howard, K.W., Zhang, J., 2009. Difficulties with Correcting Radar Rainfall Estimates Based on Rain Gauge Data: A Case Study of Severe Weather in Montana on 16-17 June 2007. *Weather and Forecasting*, 24(5): 1334-1344.
- Vasiloff, S.V. et al., 2007. Improving QPE and very short term QPF: An initiative for a community-wide integrated approach. *Bulletin of the American Meteorological Society*, 88(12): 1899-1911.
- Verdi, R.J., Holt, S.L., 2010. Floods in Florida Due to Tropical Storm Fay, August 15 Through September 26, 2008. USGS Open-File Report 2010-1142. United States Geological Survey.
- Viviroli, D. et al., 2011. Climate change and mountain water resources: overview and recommendations for research, management and policy. *Hydrology and Earth System Sciences*, 15(2): 471-504.
- Wardah, T., Abu Bakar, S.H., Bardossy, A., Maznorizan, M., 2008. Use of geostationary meteorological satellite images in convective rain estimation for flash-flood forecasting. *Journal of Hydrology*, 356(3-4): 283-298.
- Witt, A.C., 2005. Using a GIS (Geographic Information System) to model slope instability and debris flow hazards in the French Broad River watershed, North Carolina, North Carolina State University, 165 pp.
- Wooten, R.M. et al., 2008. Geologic, geomorphic, and meteorological aspects of debris flows triggered by Hurricanes Frances and Ivan during September 2004 in the Southern Appalachian Mountains of Macon County, North Carolina (southeastern USA). *Landslides*, 5(1): 31-44.

- Yildiz, O., 2001. Assessment and simulation of hydrologic extremes by a physically based spatially distributed hydrologic model. Ph.D. Thesis, The Pennsylvania State University, University Park, PA, USA.
- Yildiz, O., Barros, A.P., 2005. Climate Variability and Hydrologic Extremes-Modeling the Water and Energy Budgets in the Monongahela River Basin. *Climate and Hydrology in Mountain Areas*. Wiley.
- Yildiz, O., Barros, A.P., 2007. Elucidating vegetation controls on the hydroclimatology of a mid-latitude basin. *Journal of Hydrology*, 333(2-4): 431-448.
- Yildiz, O., Barros, A.P., 2009. Evaluating spatial variability and scale effects on hydrologic processes in a midsize river basin. *Scientific Research and Essays*, 4(4): 217-225.
- Young, C.B. et al., 1999. An evaluation of NEXRAD precipitation estimates in complex terrain. *Journal of Geophysical Research-Atmospheres*, 104(D16): 19691-19703.
- Zocatelli, D., Borga, M., Zanon, F., Antonescu, B., Stancalie, G., 2010. Which rainfall spatial information for flash flood response modelling? A numerical investigation based on data from the Carpathian range, Romania. *Journal of Hydrology*, 394(1-2): 148-161.

Table 1 - Location and elevation of raingauges referenced in this study, and the corresponding cumulative precipitation during the Fay.

NO.	Site		Lat.	Lon.	Elev.(m)	Acc.(mm)
	Site ID.	Type				
1	RG001	GSMRGN	35.40	-82.91	1156	177.79
2	RG002		35.42	-82.97	1731	163.01
3	RG003		35.38	-82.92	1609	186.19
4	RG004		35.37	-82.99	1922	214.16
5	RG005		35.41	-82.96	1520	186.32
6	RG006		35.38	-82.97	1737	186.44
7	RG007		35.46	-82.95	1478	159.20
8	RG100		35.59	-83.07	1495	127.90
9	RG101		35.58	-83.09	1520	121.32
10	RG102		35.56	-83.10	1635	103.94
11	RG103		35.55	-83.12	1688	103.73
12	RG104		35.55	-83.09	1584	58.23
13	RG105		35.64	-83.04	1345	117.31
14	RG106		35.43	-83.03	1210	112.80
15	RG107		35.57	-82.91	1359	144.19
16	RG108		35.55	-82.99	1277	123.28
17	RG109		35.50	-83.04	1500	119.60
18	RG110		35.55	-83.15	1563	123.82
19	RG111		35.73	-82.95	1394	67.94
20	RG112		35.75	-82.96	1184	95.01
21	WAYN	ECONET	35.49	-82.97	840	121.41
22	CEPN7	HADS	35.46	-82.87	818	170.43
23	CTNN7		35.55	-82.83	863	180.34
24	DARN7		35.35	-82.78	1002	239.27
25	LLDN7		35.42	-82.92	896	158.50
26	WAVN7		35.43	-83.01	943	114.81
27	WLTN7		35.70	-83.04	735	101.09

Table 2 – Summary of the RMSE computed from observed rainfall rate (mm/hr) and Q2 product before and after adjustment.

	RMSE(mm/hr)			
QPE	GSMRGN	ECONET	HADS	All
Q2	2.00	1.67	2.78	2.18
Q2+_All	1.35	0.85	1.44	1.35
Q2+_H/L	1.19	0.88	0.93	1.13

Table 3 – Major parameters specified in LSHM for three soil layers.

	CCB	WFPRB	EFPRB
Soil Geometry(m)	0.15-0.50-0.80	0.05-0.30-0.50	0.10-0.30-0.50
K_{sat} (min.~max.)	0.9~2.8×10 ⁻⁵ m/s	0.9~2.8×10 ⁻⁵ m/s	0.9~2.8×10 ⁻⁵ m/s
Porosity (min.~max.)	0.43~0.49	0.48~0.51	0.48~0.51
Field Capacity (min.~max.)	0.16~0.26	0.21~0.22	0.21~0.26
Wilting Point (min.~max.)	0.081~0.163	0.09~0.13	0.09~0.16

Table 4 – Error Summary of QFE (nowcast) performance[#]

Basin	Forcing Rainfall Datasets	Time-to-Peak (hr.) [Error=(T _p ^{est} - T _p ^{obs})]	Peak Flow (%)* [Error=(Q _p ^{est} - Q _p ^{obs})/ Q _p ^{obs}]	Flow Vol (%)* [Error=(V _{est} -V _{obs})/ V _{obs}]	Flow Apportionment (%)		
					Overland	Interflow	Baseflow
CCB	Q2	5.83	-92.27	-60.36	0.13	12.62	87.25
	Q2+_All	-0.17	-7.20	-4.66	3.30	59.01	37.69
	Q2+_H/L	-0.33	2.59	0.34	3.97	60.35	35.68
WFPRB ⁺	Q2	-0.83	-77.66	-86.93	20.02	42.08	37.90
	Q2+_All	1.08	8.33	-0.17	39.21	56.02	4.77
	Q2+_H/L	1.00	19.74	-0.94	38.02	57.13	4.85
EFPRB	Q2	17.33	-99.48	-95.66	0.00	19.93	80.07
	Q2+_All	0.58	11.69	2.54	24.08	72.39	3.53
	Q2+_H/L	0.67	0.91	1.87	25.77	70.53	3.70

[#]The error index indicating the best performance of QFEs for each term is highlighted in bold.

*Negative values indicate underestimation and positive values mean overestimation.

⁺There are double peaks for the WFPRB, the calculations were performed with respect to the major peak.

Table 5 – Error Index of QFE (nowcast) performance

Basins	WFPRB			EFPRB		
QFE By:	RMSE	RSR	NSE	RMSE	RSR	NSE
Q2	31.97	1.07	-0.15	39.94	1.22	-0.49
Q2+_All	12.60	0.42	0.82	12.47	0.38	0.86
Q2+_H/L	13.78	0.46	0.79	10.50	0.32	0.90

Figure 1 – Topography, major rivers and raingauges over Pigeon River basin in North Carolina. The CCB (Cataloochee Creek Basin), WFPRB (West Fork Pigeon River Basin) and EFPRB (East Fork Pigeon River Basin) are illustrated by black polygons. [ECONET - Environment and Climate Observing Network; HADS - Hydrometeorology Automated Data System; PMM GSMRGN - Precipitation Measuring Mission (PMM) rain-gauge network in the Great Smoky Mountains; MRR - MicroRain Radar.]

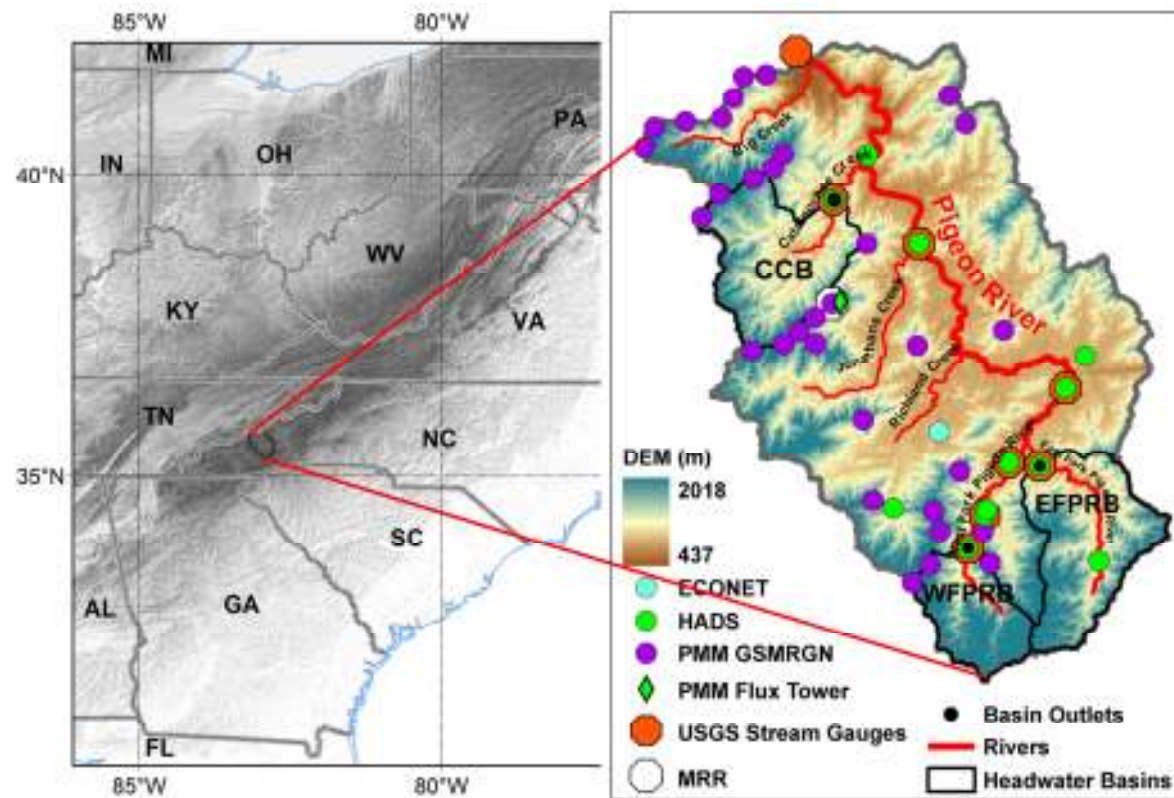


Figure 2 – Soil texture (left) derived from STATSGO and land cover map (right) derived from National Land Cover Database (NLCD) over Haywood County. CCB, WFPRB and EFPRB are illustrated by cyan polygons.

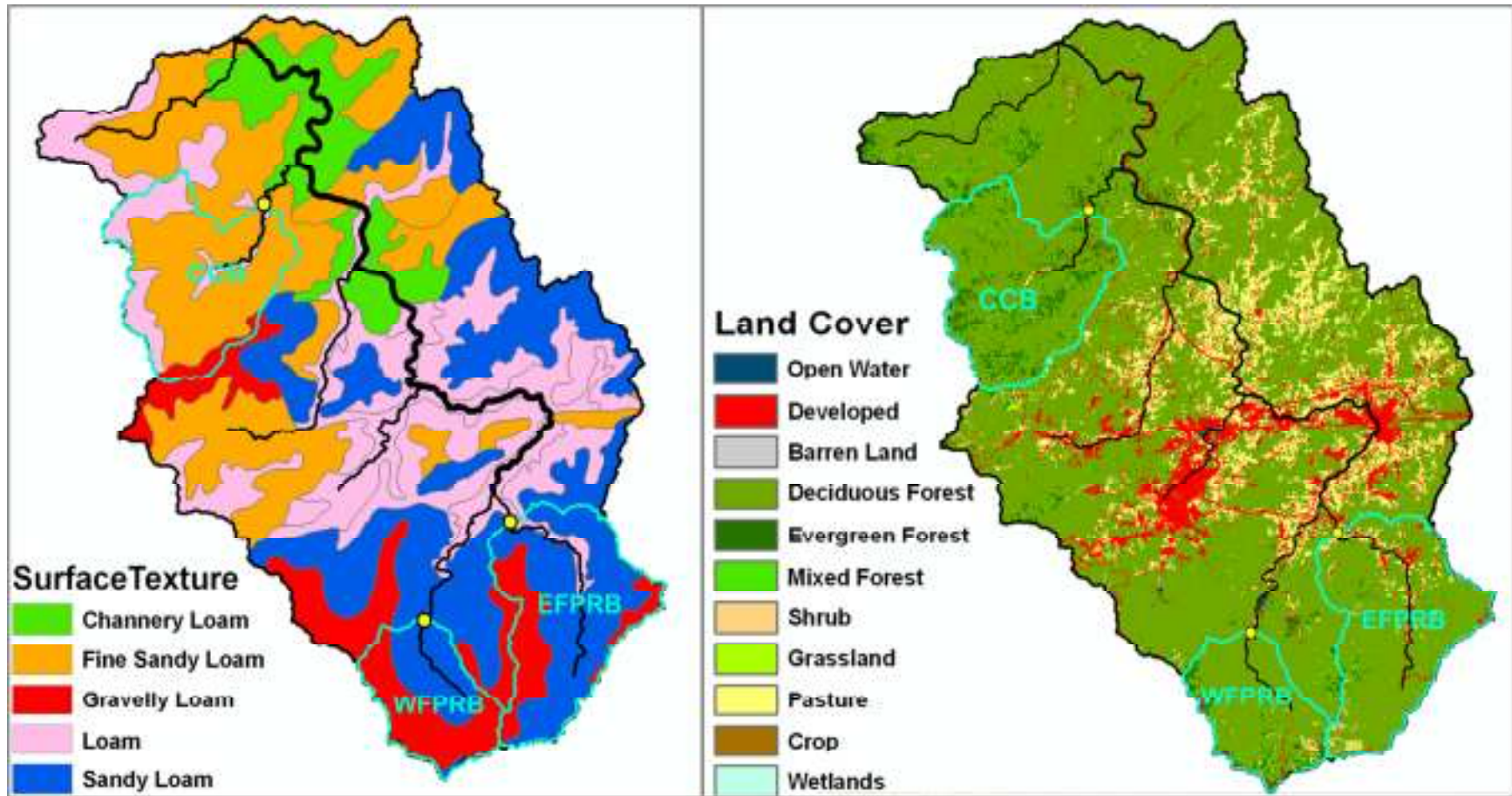


Figure 3 - Comparison between rain-gauge observations and Q2 (a.*), Q2+_All (b.*), and Q2+_H/L (c.*) during Tropical Storm Fay.

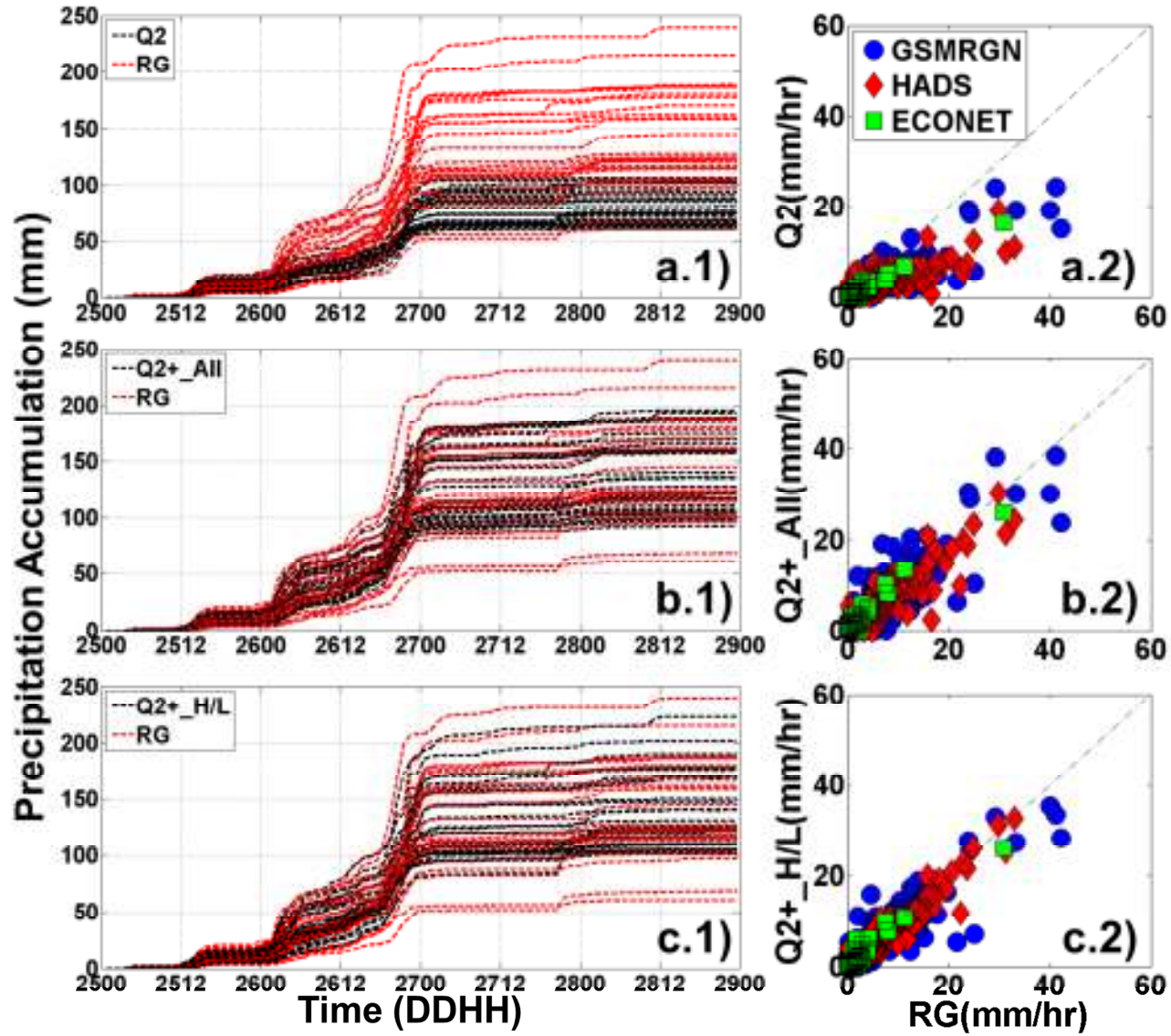


Figure 4 – Spatial distribution of precipitation accumulation for Q2 (a), Q2+_All (b) and Q2+_H/L (c) during Tropical Storm Fay (Aug.25-28, 2008).

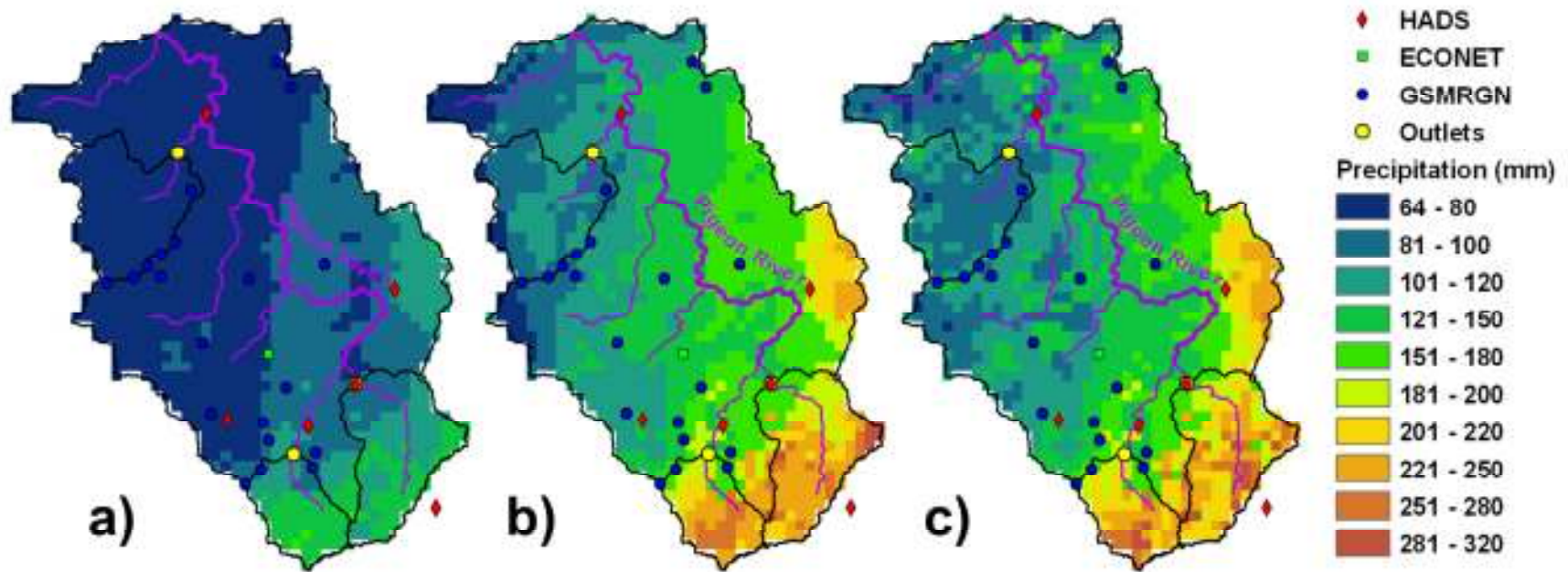


Figure 5 – Six-hourly QPF accumulation for 12:00~18:00 (UTC) on August 26, 2008, provided by NDFD. Note that even though NDFD updates national mosaic hourly, the new information was incorporated into QPF by WFO at 09:00AM. The Pigeon River is the basin with the marked river network.

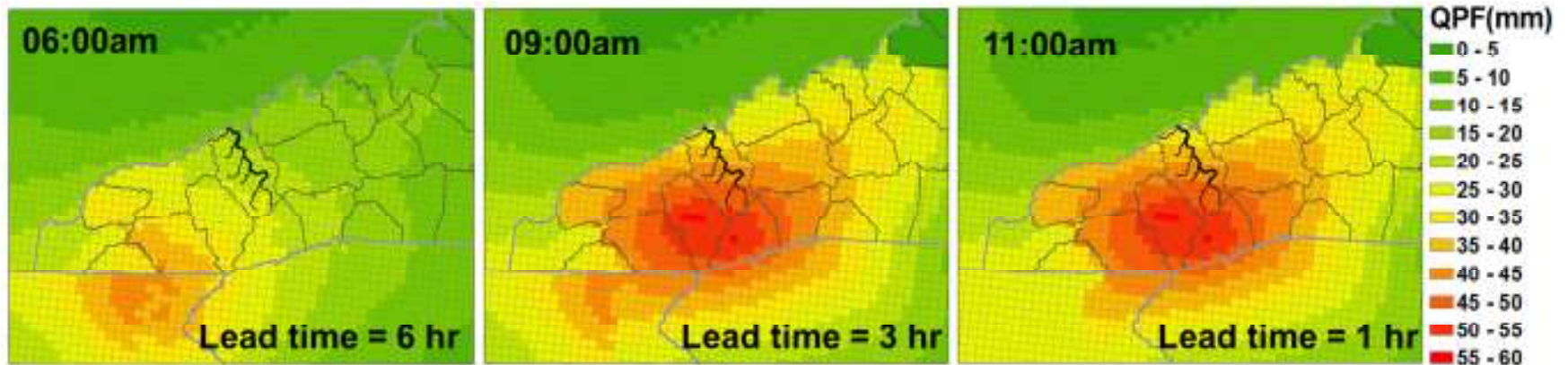


Figure 6 – Six-hourly QPF accumulation with one hour lead time on August 26 (left) and August 27 (right), 2008.

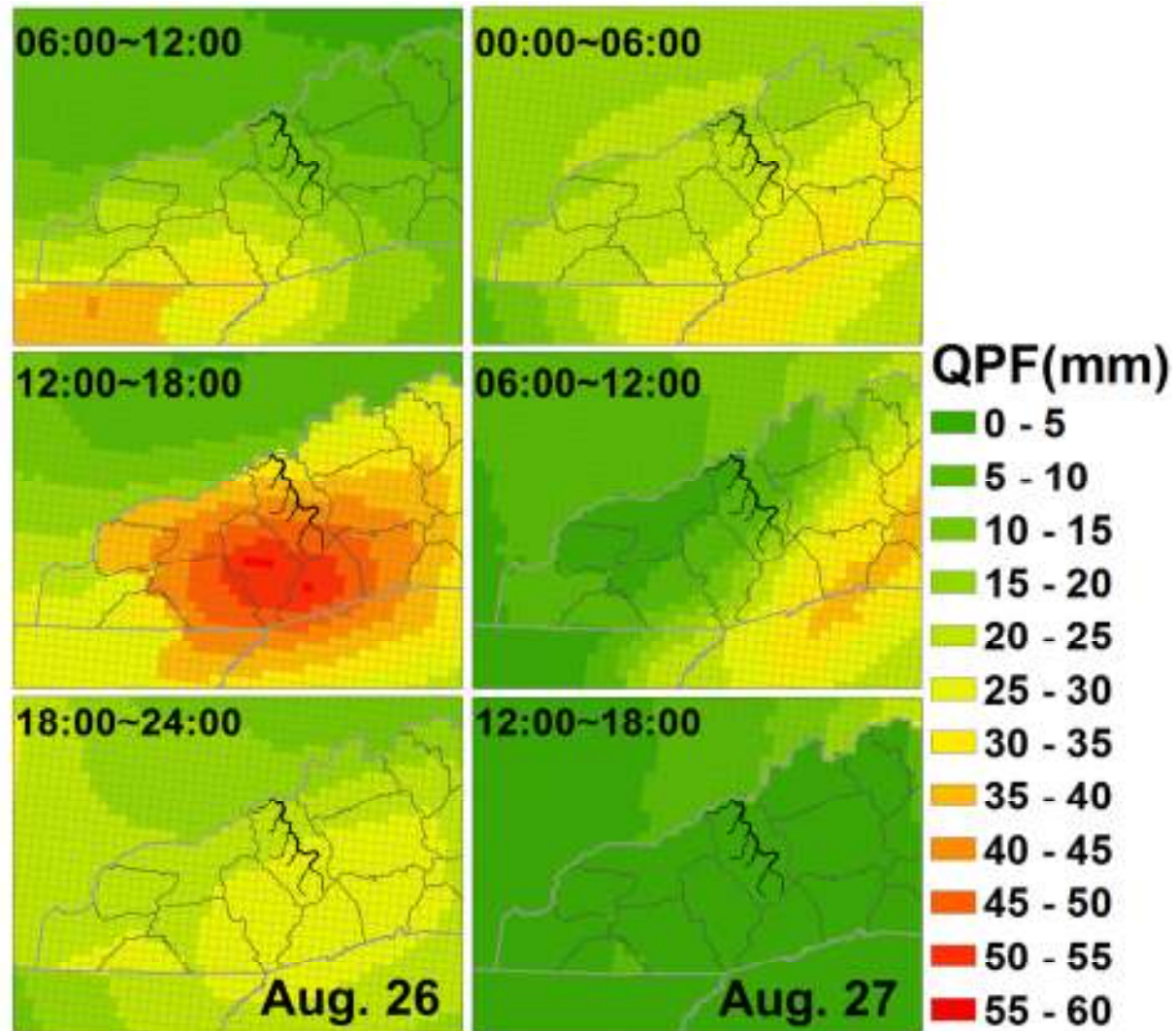


Figure 7 – Comparison between areal averaged six-hour QPF and Q2 datasets over Haywood County, including Q2 and Q2+ datasets. Time axis represents date and the beginning of forecast period (DDHH). The upper plot shows 6-hr lead time QPF (a), the bottom plot shows 1-hr lead time QPF (b). The embedded figure shows comparison between 1-hr lead time six-hour QPFs and the averaged six-hour rainfall amount observed by the raingauges located in the corresponding QPF grids.

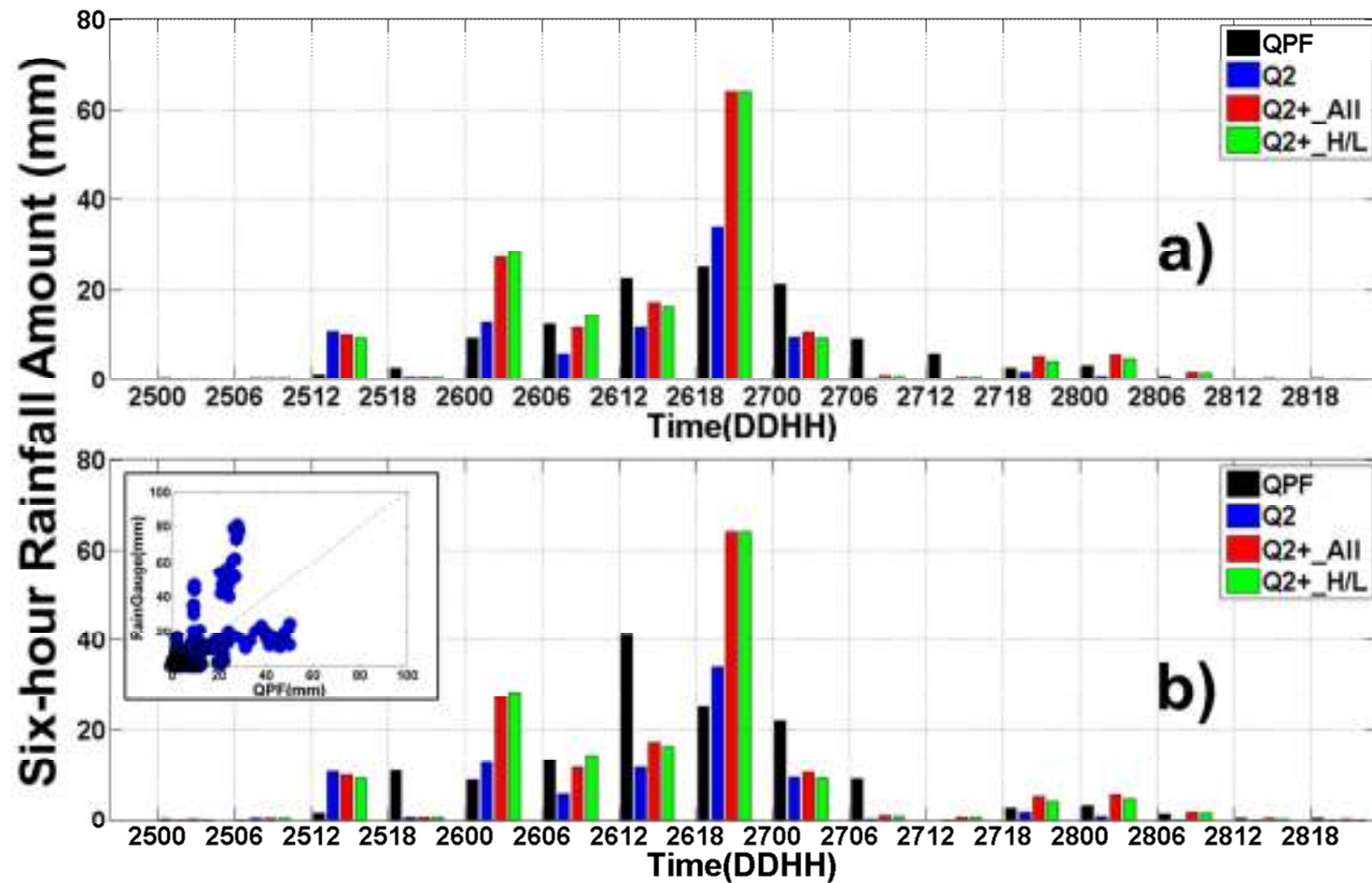


Figure 8 – Comparison between six-hour QPF and Q2 datasets at NDFD pixels (5km) over the Haywood County area. The left panel shows the 6-hr lead time QPF (a), while the right panel shows the 1-hr lead time QPF (b). The pink numbers indicate the selected six-hour QPF time (DDHH) corresponding to the symbols.

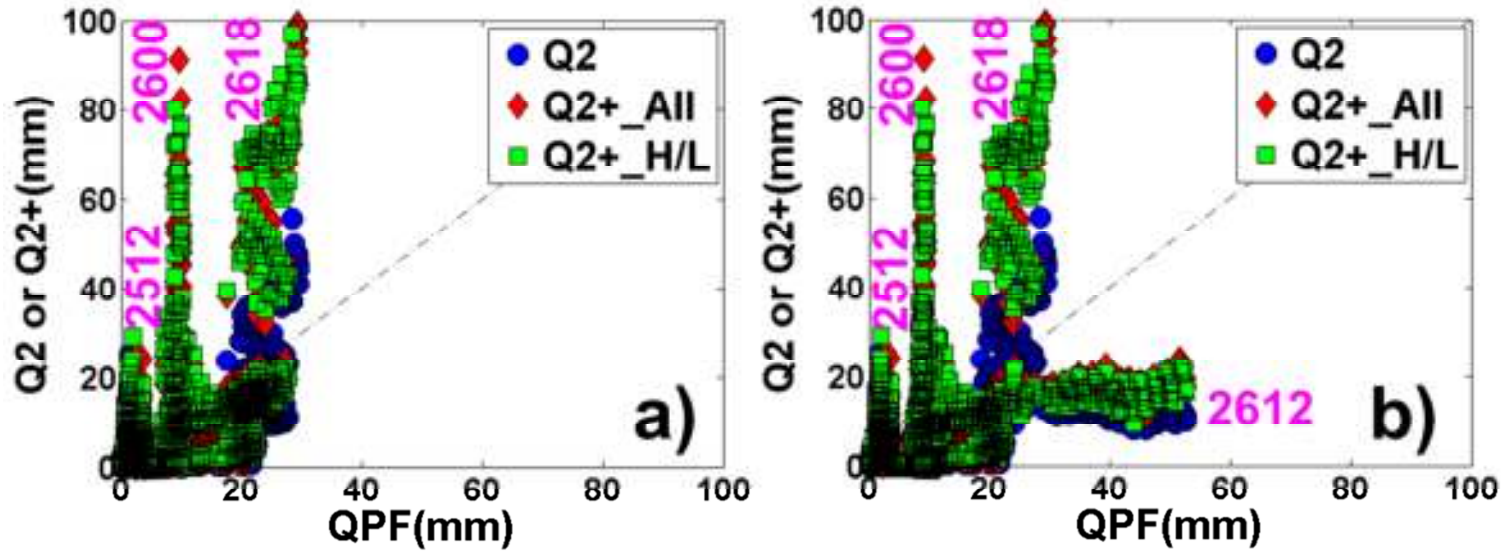


Figure 9 – The conceptual configuration of reconstructing rainfall fields for QFF, where QPE can be Q2 or Q2 incorporated available GPM products.

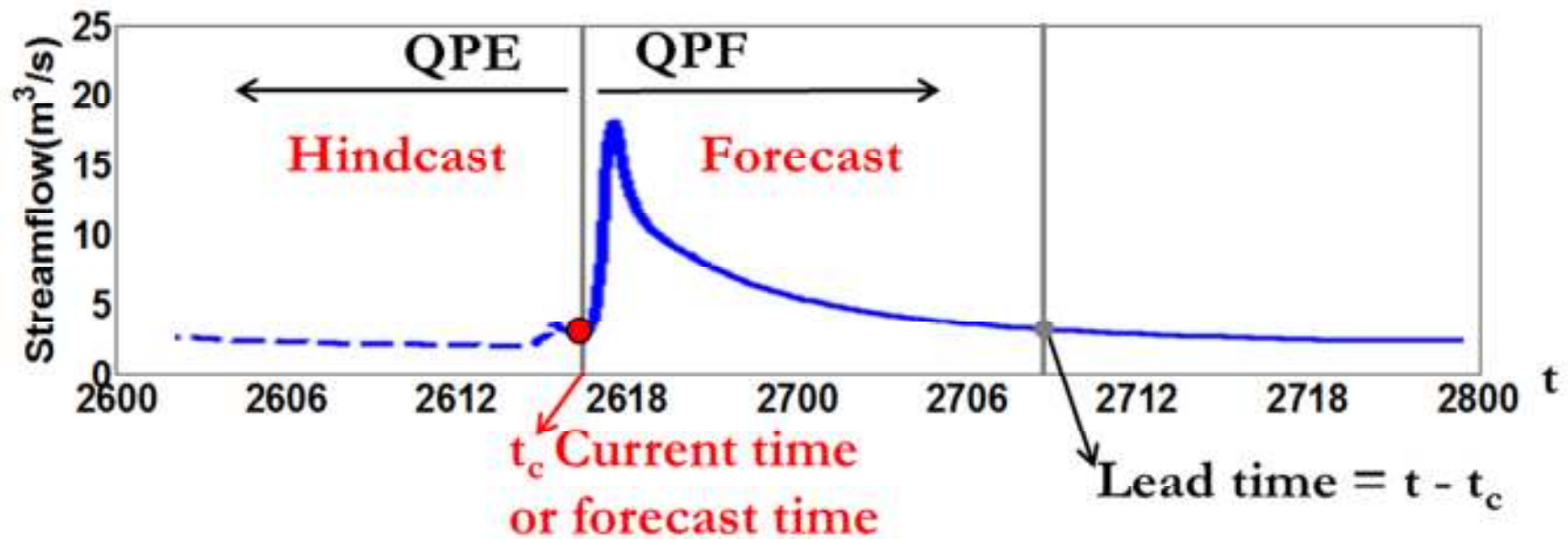


Figure 10 – The comparison between QFEs over the CCB generated from the 3D-LSHM driven by three different rainfall datasets are shown in (a); the flow components of estimated streamflow forced by Q2+_H/L are shown in (b). The upper and right axis in (b) indicate basin areal averaged storm hyetograph.

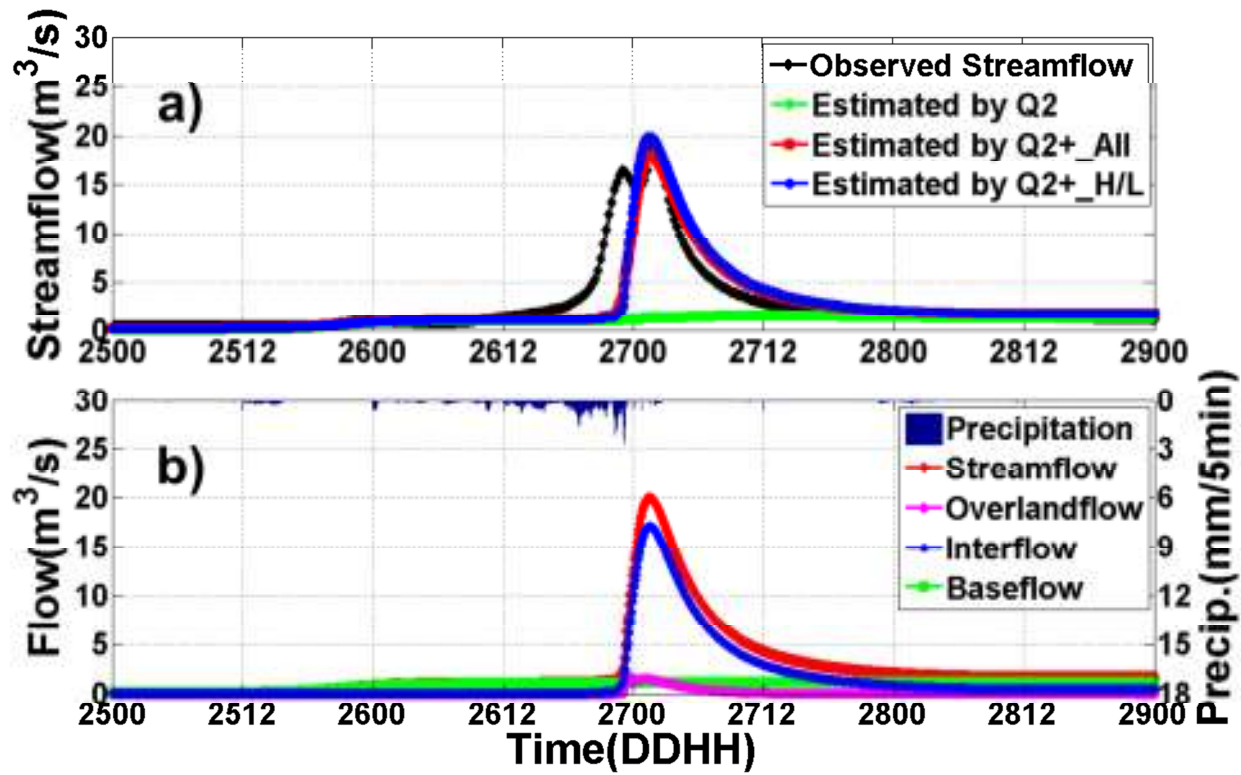


Figure 11 – The comparison between QFEs over the WFPRB generated from the 3D-LSHM driven by three different rainfall datasets are shown in (a); the flow components of estimated streamflow forced by Q2+_All are shown in (b). The upper and right axis in (b) indicate basin areal averaged storm hyetograph.

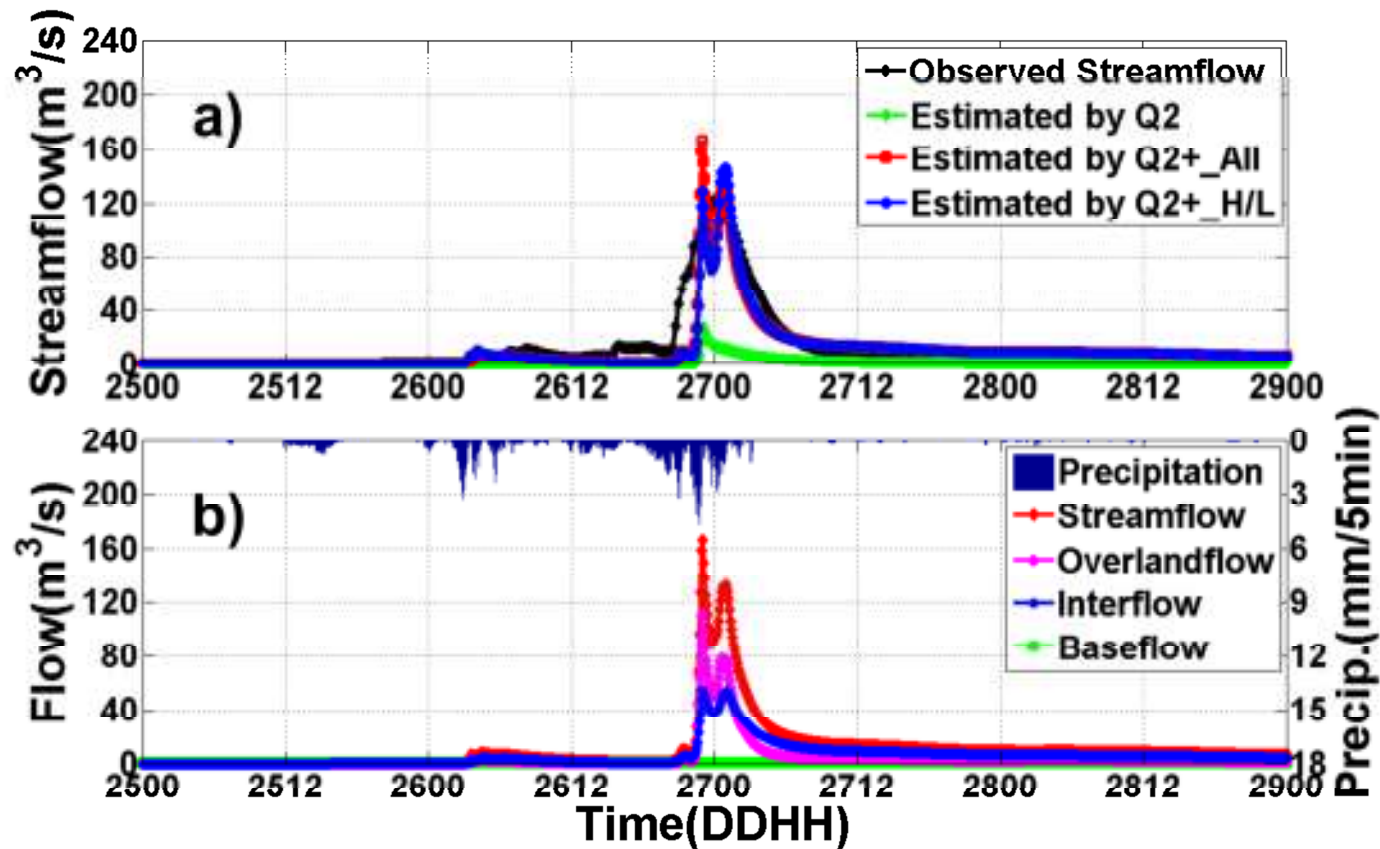


Figure 12 – The comparison between QFEs over the EFPRB generated from the 3D-LSHM driven by three different rainfall datasets are shown in (a); the flow components of estimated streamflow forced by Q2+_H/L are shown in (b). The upper and right axis in (b) indicate basin areal averaged storm hyetograph.

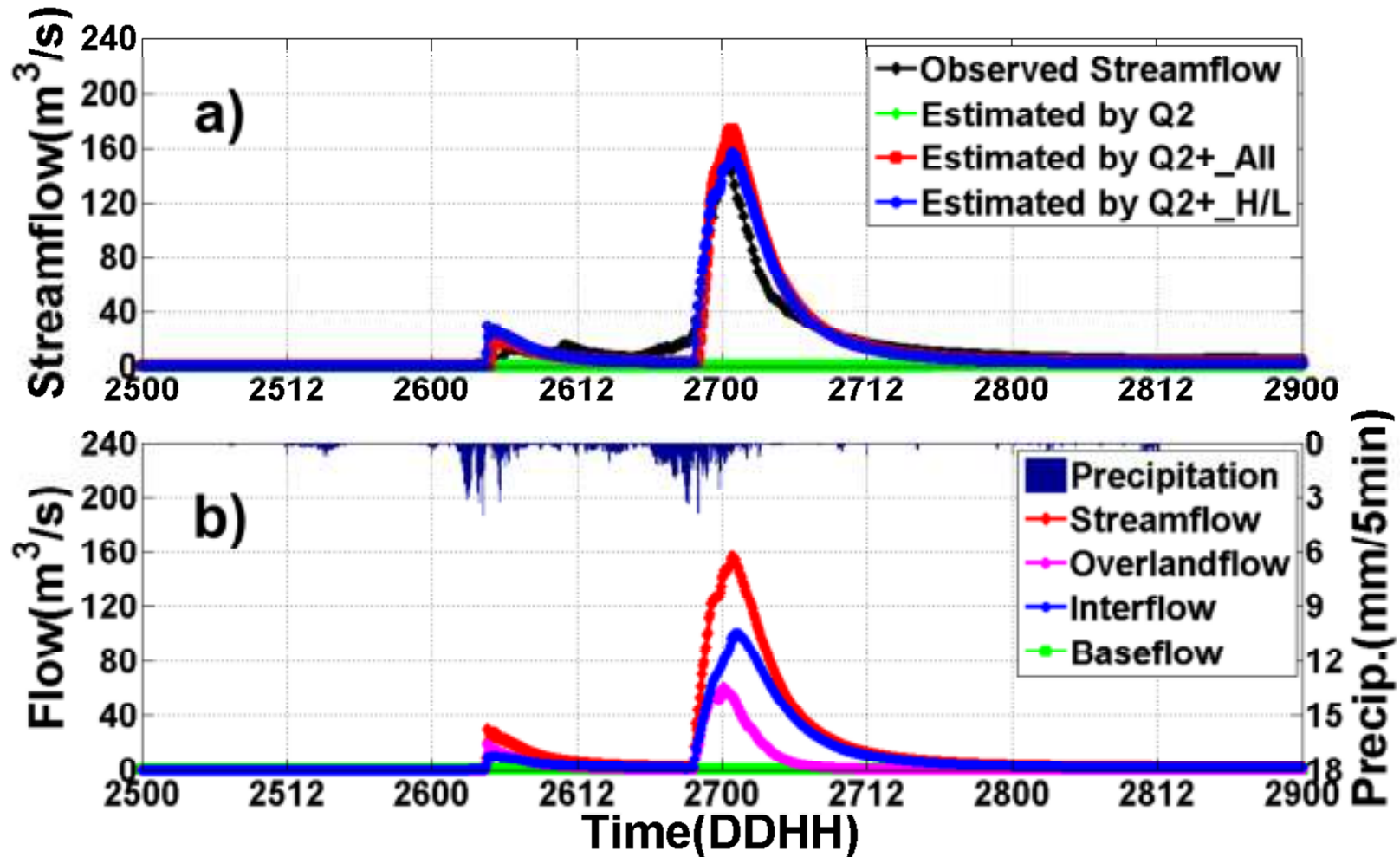


Figure 13 – Example of rainfall uncertainty for Q2+_All (a) and Q2+_H/L (b) associated with regression models at each hour; smaller symbols indicate the rainfall replicates sampled from the 95% confidence intervals of regression models.

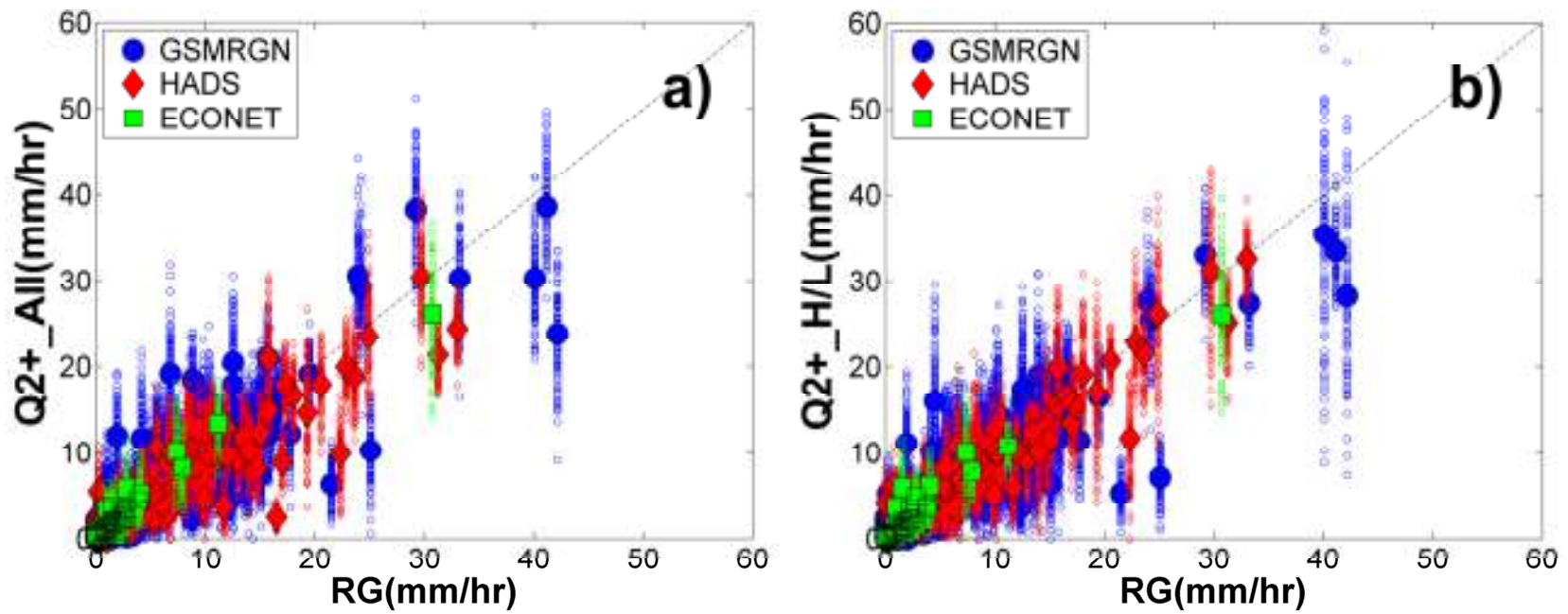


Figure 14 – The observed hydrographs (black) and simulated QFEs (red) forced by Q2+_All in left panel (a and c) and Q2+_H/L in right panel (b and d) over the WFPRB (upper) and EFPRB (lower); The ensembles of simulated QFEs forced by rainfall replicates are indicated by blue dash lines; Shaded gray, green and yellow areas are the uncertainty estimates of simulated streamflow for the 95%, 70% and 50% confidence intervals (CI), respectively.

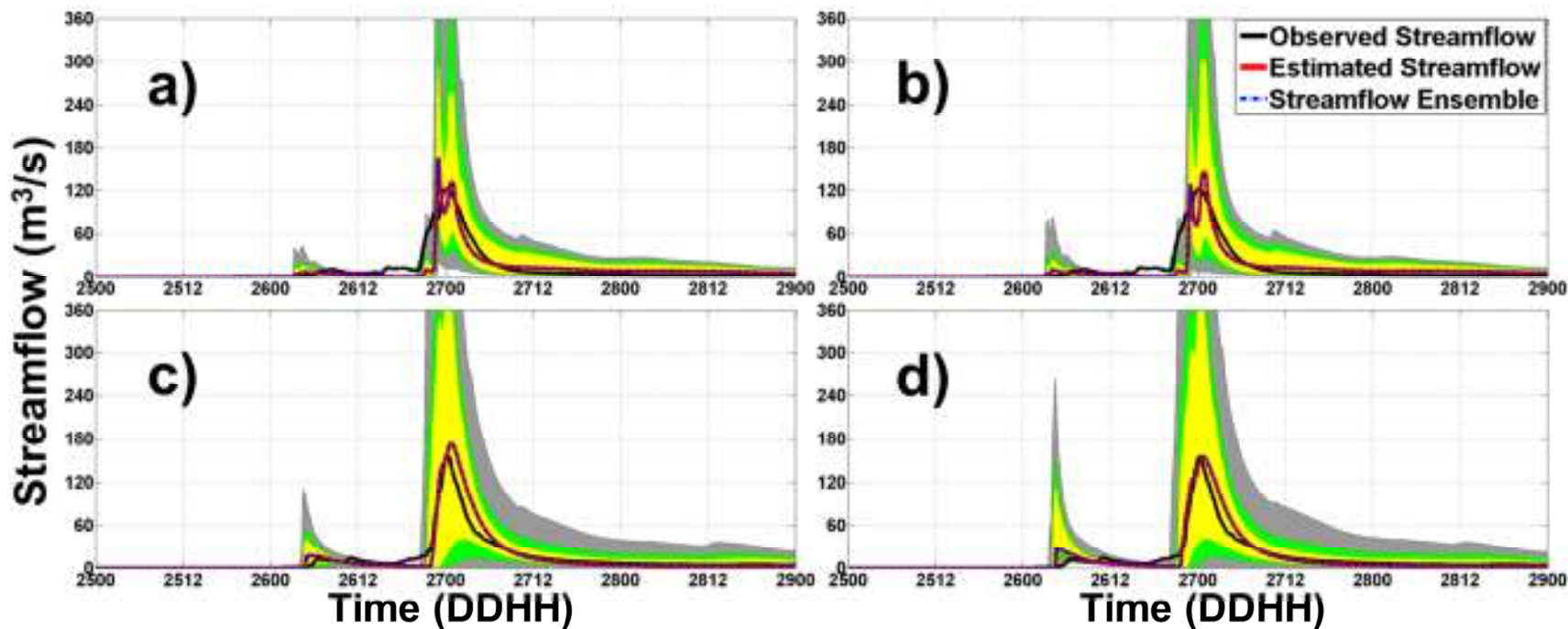


Figure 15 – Relative errors in peak flow versus the corresponding RMSE of rainfall replicates sampled from 95%, 70% and 50% confidence interval (CI) associated with Q2+_All (a and c) and Q2+_H/L (b and d) over the WFPRB (upper) and EFPRB (lower).

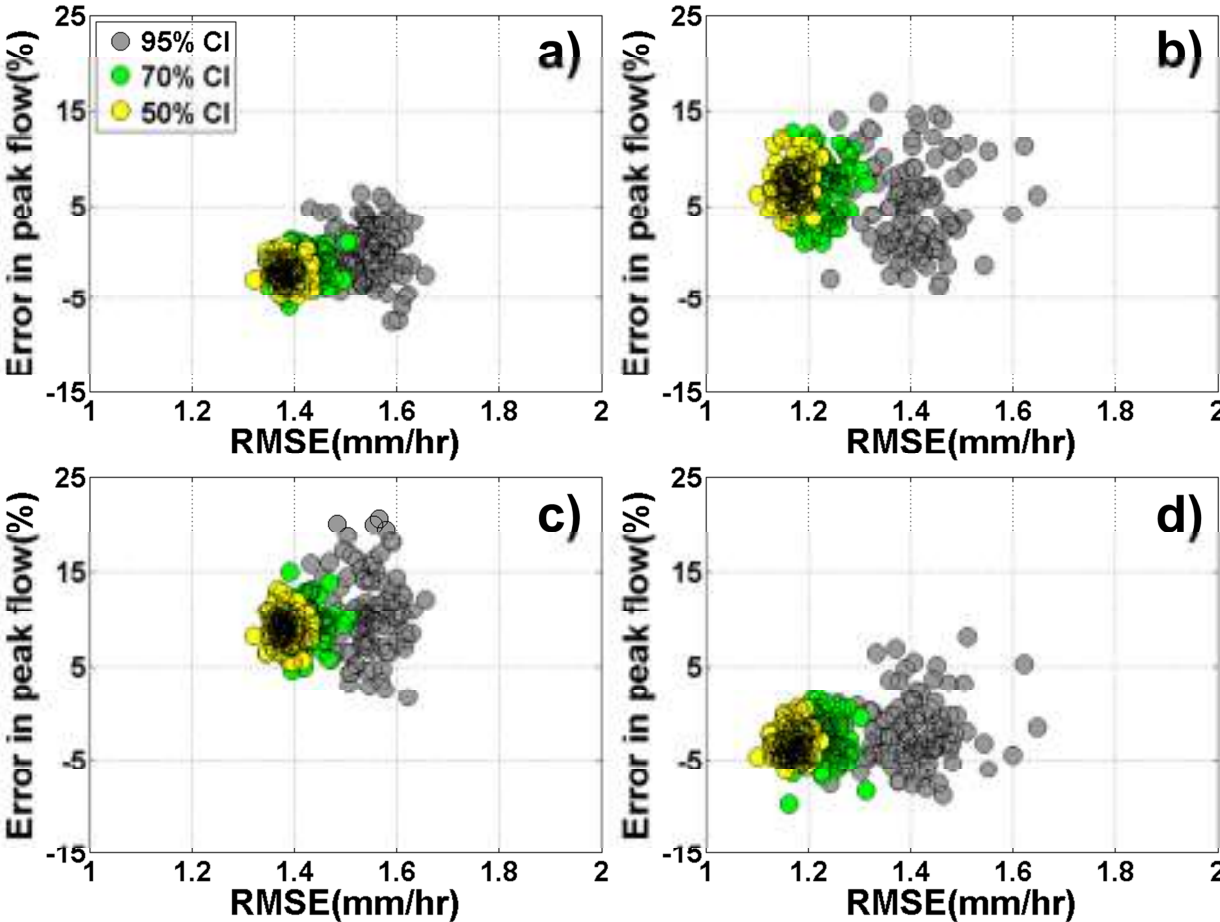


Figure 16 – The combination of Q2 with simulated GPM rainfall sampling from Q2+_All over the WFPRB (a), and with simulated GPM rainfall sampling from Q2+_H/L over the EFPRB (b). GPM# refers to the three different 3-hour sampling schemes indicated by green, blue and red lines.

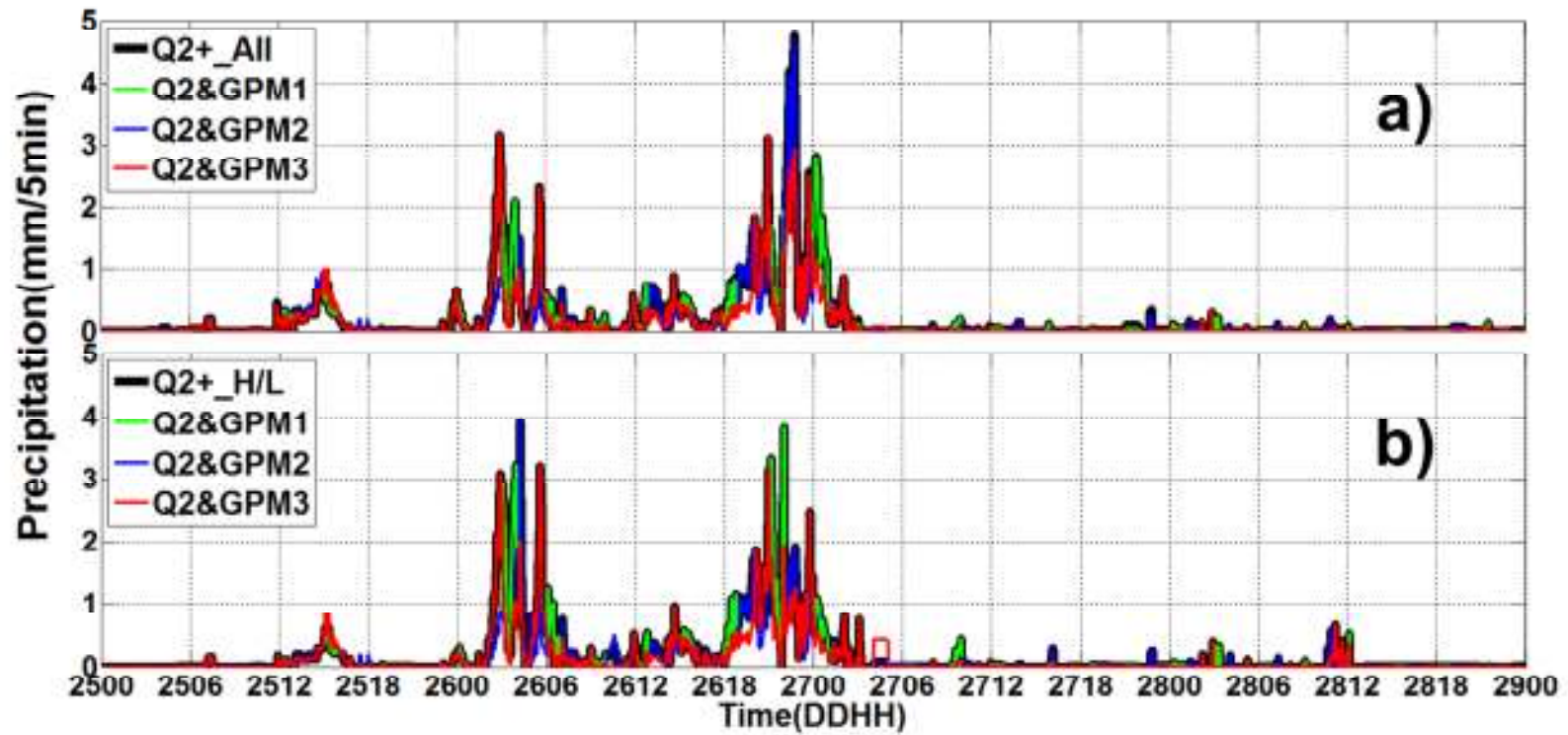


Figure 17 – Quantitative Flash-Flood Forecasts (QFFs) by 3D-LSHM driven by the combination of Q2&GPM#+QPF over the WFPRB. GPM were obtained by sampling the Q2+_All dataset. Two QFFs made at 12:00am on 26 Aug. and 00:00am on 27 Aug. are shown by a) and b) respectively.

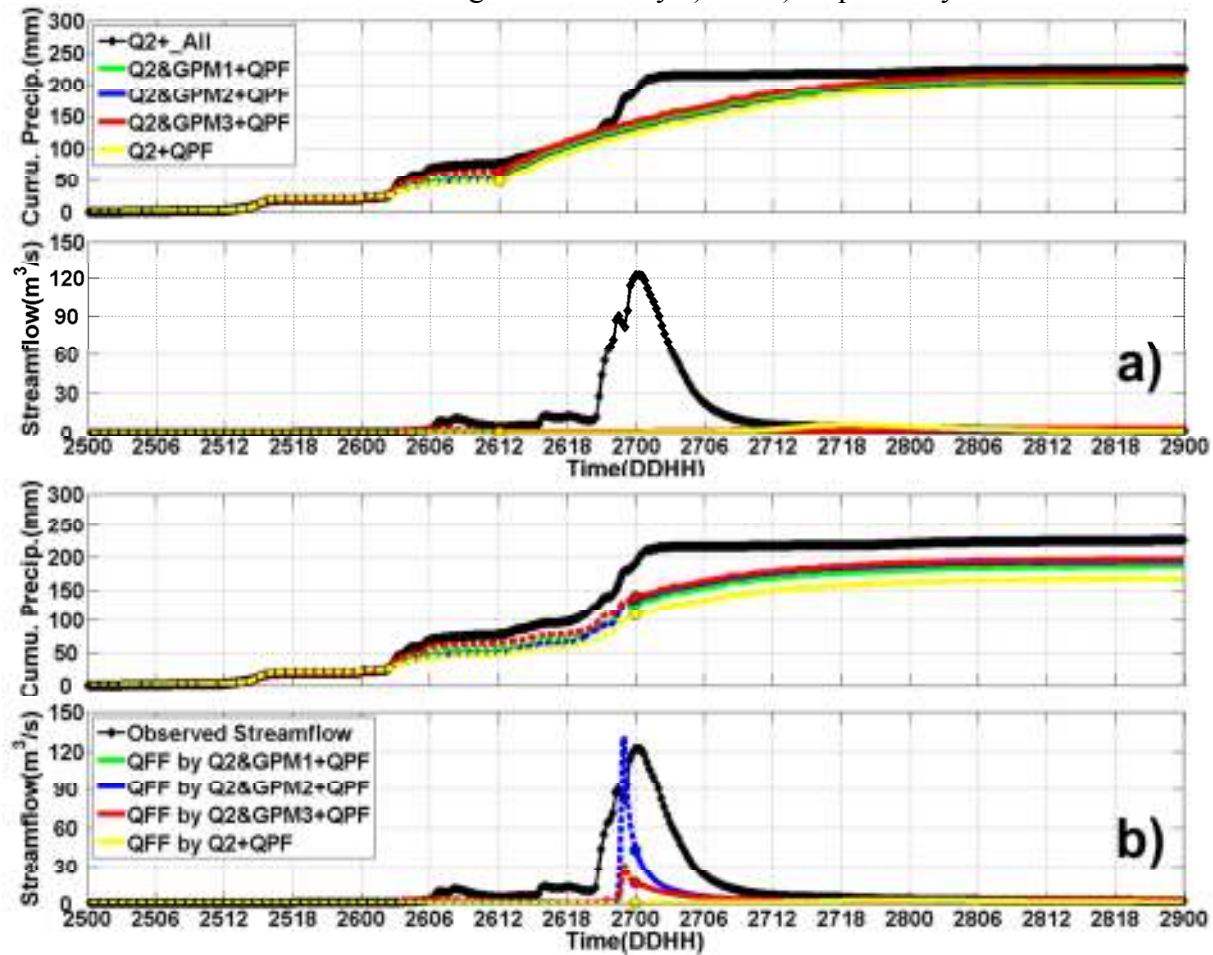


Figure 18 – Quantitative Flash-Flood Forecasts (QFFs) by 3D-LSHM driven by the combination of Q2&GPM#+QPF over the EFPRB. GPM were obtained by sampling the Q2+_H/L dataset. Two QFFs made at 12:00am on 26 Aug. and 00:00am on 27 Aug. are shown by a) and b) respectively.

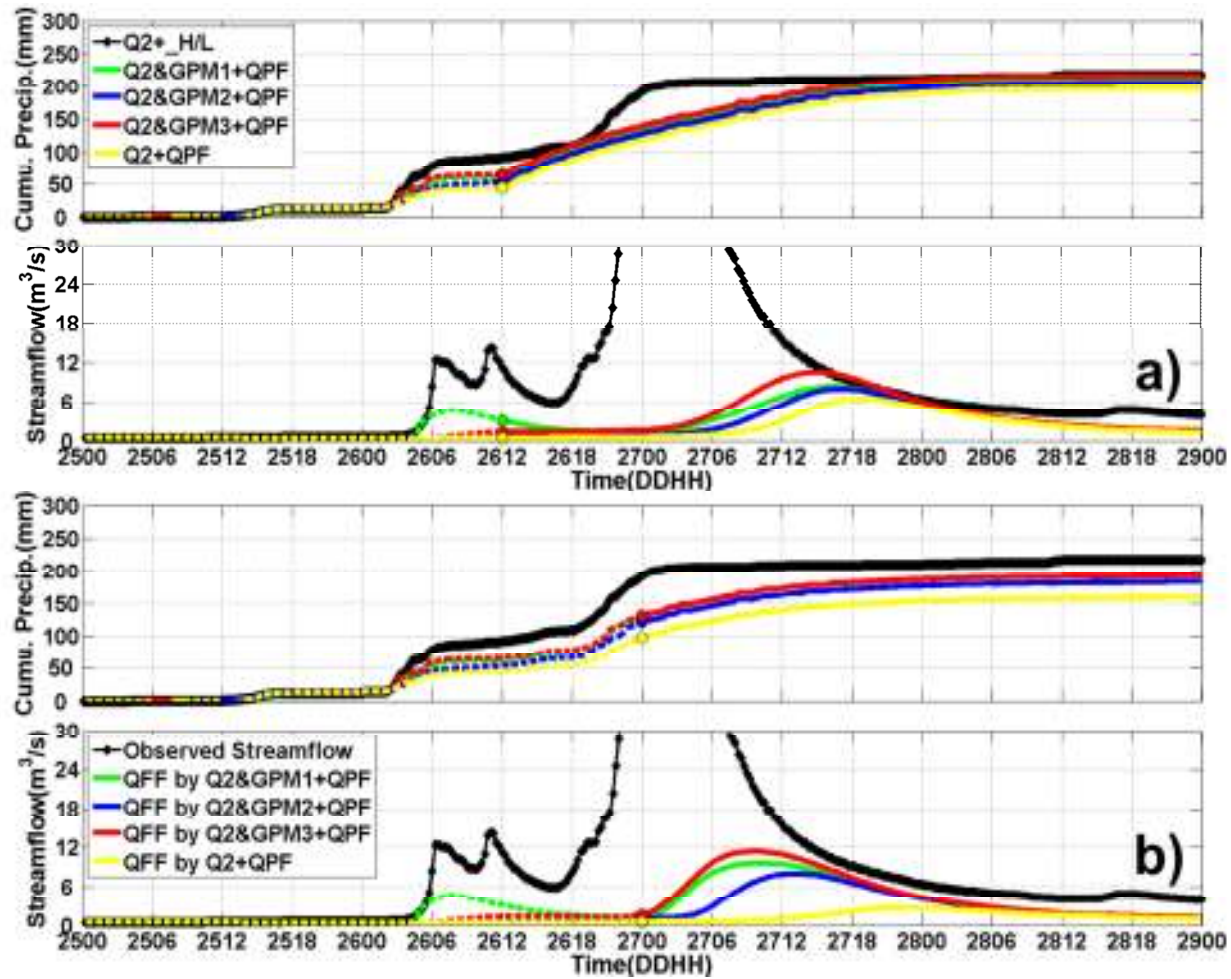


Figure 19 – Error statistics for QFF including RMSE, RSR and NSE for different lead times over the WFPRB (left) and EFPRB (right), calculated using 15min time-series.

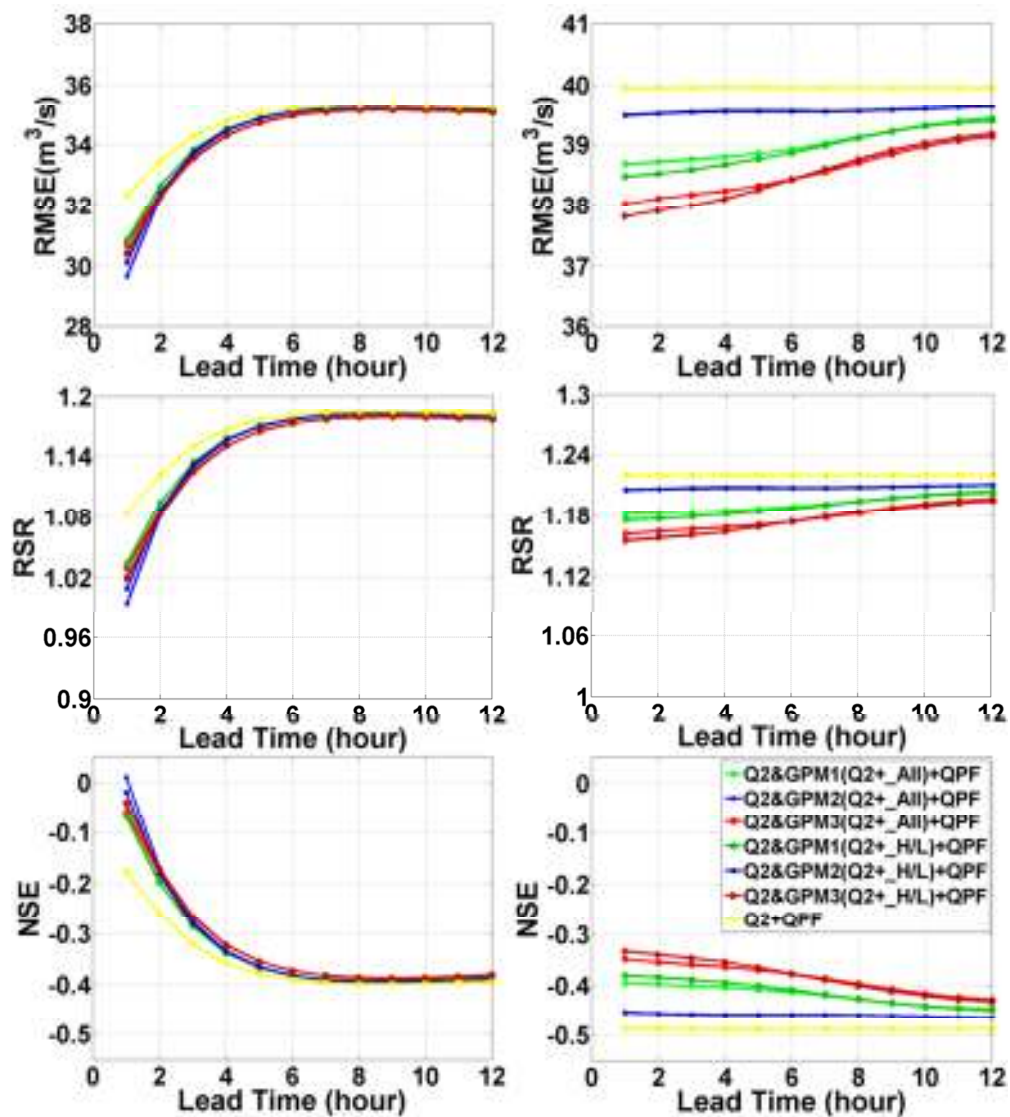
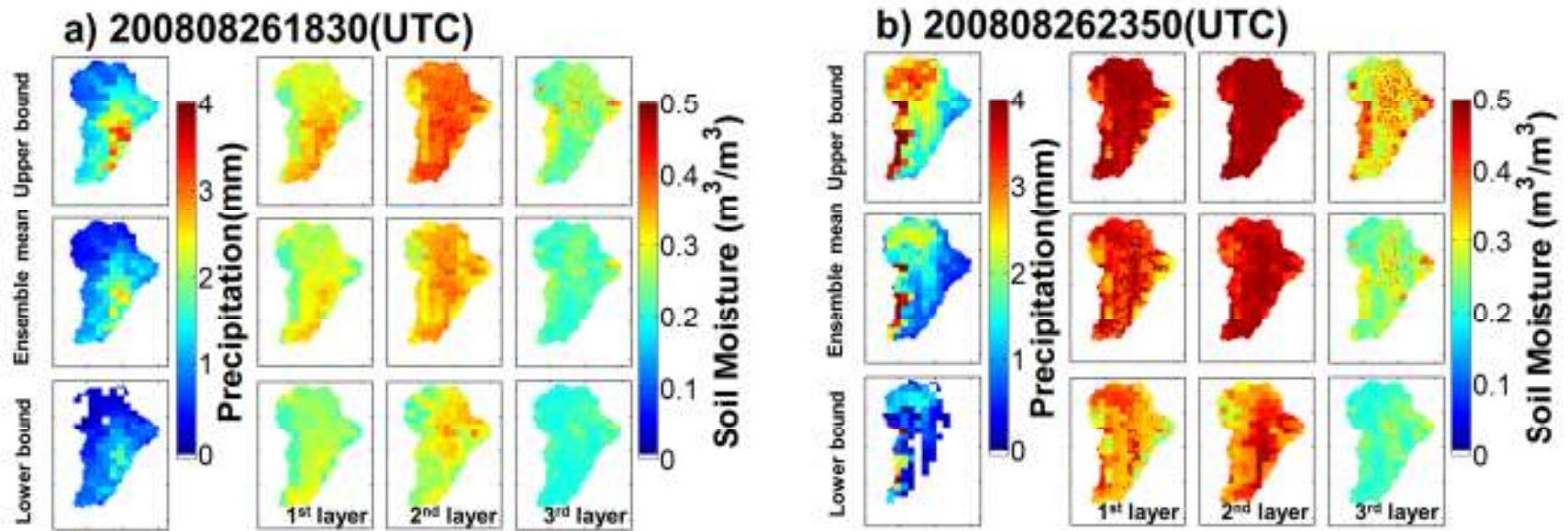


Figure 20 – Spatial rainfall for the 70% CI upper and lower bounds, and ensemble mean for the Monte Carlo simulations over the EFPRB at two selected times (a and b); and the corresponding soil moisture fields simulated in the top three layers.



Copyright Duke University 2012